Contents lists available at ScienceDirect

Remote Sensing of Environment

journal homepage: www.elsevier.com/locate/rse

Mapping actual evapotranspiration using Landsat for the conterminous United States: Google Earth Engine implementation and assessment of the SSEBop model

Gabriel B. Senay [a,*], MacKenzie Friedrichs [b], Charles Morton [c], Gabriel E.L. Parrish [d], Matthew Schauer [e], Kul Khand [f], Stefanie Kagone [f], Olena Boiko [b], Justin Huntington [c]

[a] *U.S. Geological Survey (USGS), Earth Resources Observation and Science (EROS) Center, North Central Climate Adaptation Science Center, Fort Collins, CO 80523, USA*
[b] *KBR – Contractor to the U.S. Geological Survey (USGS), Earth Resources Observation and Science (EROS) Center, Sioux Falls, SD 57198, USA*
[c] *Desert Research Institute (DRI), Reno, NV 89512, USA*
[d] *Innovate! Inc. – Contractor to the U.S. Geological Survey (USGS), Earth Resources Observation and Science (EROS) Center, Sioux Falls, SD 57198, USA*
[e] *C2G Inc. – Contractor to the U.S. Geological Survey (USGS), Earth Resources Observation and Science (EROS) Center, Sioux Falls, SD 57198, USA*
[f] *ASRC Federal Data Solutions – Contractor to the U.S. Geological Survey (USGS), Earth Resources Observation and Science (EROS) Center, Sioux Falls, SD 57198, USA*

ARTICLE INFO

ABSTRACT

The estimation and mapping of actual evapotranspiration (ETa) is an active area of applied research in the fields of agriculture and water resources. Thermal remote sensing-based methods, using coarse resolution satellites, have been successful at estimating ETa over the conterminous United States (CONUS) and other regions of the world. In this study, we present CONUS-wide ETa from Landsat thermal imagery-using the Operational Simplified Surface Energy Balance (SSEBop) model in the Google Earth Engine (GEE) cloud computing platform. Over 150,000 Landsat satellite images were used to produce 10 years of annual ETa (2010–2019) at unprecedented scale. The accuracy assessment of the SSEBop results included point-based evaluation using monthly Eddy Covariance (EC) data from 25 AmeriFlux stations as well as basin-scale comparison with annual Water Balance ETa (WBET) for more than 1000 sub-basins. Evaluations using EC data showed generally mixed performance with weaker ($R^2 < 0.6$) correlation on sparsely vegetated surfaces such as grasslands or woody savanna and stronger correlation ($R^2 > 0.7$) over well-vegetated surfaces such as croplands and forests, but location-specific conditions rather than cover type were attributed to the variability in accuracy. Croplands performed best with R^2 of 0.82, root mean square error of 29 mm/month, and average bias of 12%. The WBET evaluation indicated that the SSEBop model is strong in explaining the spatial variability (up to $R^2 > 0.90$) of ETa across large basins, but it also identified broad hydro-climatic regions where the SSEBop ETa showed directional biases, requiring region-specific model parameter improvement and/or bias correction with an overall 7% bias nationwide. Annual ETa anomalies over the 10-year period captured widely reported drought-affected regions, for the most part, in different parts of the CONUS, indicating their potential applications for mapping regional- and field-scale drought and fire effects. Due to the coverage of the Landsat Path/Row system, the availability of cloud-free image pixels ranged from less than 12 (mountainous cloud-prone regions and U.S. Northeast) to more than 60 (U.S. Southwest) per year. However, this study reinforces a promising application of Landsat satellite data with cloud-computing for quick and efficient mapping of ETa for agricultural and water resources assessments at the field scale.

1. Introduction

The estimation and mapping of evapotranspiration (ET) is an active area of applied research in agriculture and water resources. Landscape ET represents the combined processes of evaporation and transpiration by which water is transferred from the soil-water-vegetation system to

---

the atmosphere thereby completing the hydrologic cycle through the movement of water and energy.

The science and instrumentation of measuring ET at the field scale has been well-established over decades of research using devices such as lysimeters (Allen et al., 1991), Eddy Covariance (EC) stations (Baldocchi et al., 2001), Bowen ratio (Bowen, 1926), and sap flow (Vertessy et al., 1997) techniques. But the estimation of ET over large areas has only been possible with the advent of satellite data. Although ET is a difficult process to directly quantify because of its gaseous phase, the fact that it occurs continuously over space and time, i.e., throughout the day over a landscape, makes ET conducive to observation and measurement using polar orbiting satellites that can only take an infrequent instantaneous measurement.

While satellite data brings great opportunities to cover large areas for actual evapotranspiration (ETa) estimation, remote sensing ETa also faces two main challenges. The first challenge is that complex algorithms must be developed to account for complex spatiotemporal variations and confounding factors so that landscape ETa could be estimated with desired accuracy and consistency over space and time. The second challenge is the application of complex ETa models using Landsat-scale satellite data is computationally intensive because of the large quantity and file sizes of satellite images and associated weather variables. Therefore, even satellite-based estimation is generally limited to study areas and timeframes that allow ETa modeling with small-scale computing infrastructure. Continental and global scale estimation of ETa has been restricted to the use of coarse resolution satellite data streams such as the Moderate Resolution Imaging Spectroradiometer (MODIS) (Guerschman et al., 2009; Mu et al., 2011; Zheng et al., 2016; FAO, 2018; Senay et al., 2020), Advanced Very High Resolution Radiometer (Fisher et al., 2008) or those derived from geostationary satellites (Anderson et al., 2007; Alemohammad et al., 2017).

To obtain Landsat-scale ETa, researchers have used a multi-sensor approach where Landsat and coarser datasets are combined to estimate moderate-resolution Landsat-scale ETa. The fusion of Landsat and MODIS serves the purpose of improving the temporal coverage of Landsat using a high frequency data from MODIS. A successful merging of Landsat and MODIS has been shown to improve ETa estimation at a regional and field level (Nagler et al., 2012; Singh et al., 2014; Ke et al., 2017; Sun et al., 2017; Yang et al., 2018; Jiang et al., 2020).

In addition to combined products, Landsat-based ETa products have been developed and evaluated over a range of scales from field to basin-wide applications around the world. Irmak et al. (2011) demonstrated the application of the Mapping EvapoTranspiration at high Resolution with Internalized Calibration (METRIC) model by Allen et al. (2007) for predicting field-scale corn water use in Nebraska, USA using Landsat data and concluded that the method was viable to scale over large areas in humid environments with proper calibrations.

Choi et al. (2009) compared three energy balance models [METRIC (Allen et al., 2007), Two Source (Kustas and Norman, 2000), and Trapezoid Interpolation method (Jiang and Islam, 2001)] over corn and soybean fields in Iowa, USA using Landsat and reported discrepancies among models over large areas, despite good agreements with EC data, highlighting the challenges of modeling ETa consistently over large areas. Successful applications of Landsat data for other land cover types such as grasslands and forests have been documented by several researchers (Sun et al., 2011; Li et al., 2013; Numata et al., 2017; Khand et al., 2017; Yang et al., 2020), but these studies are limited to watershed- or sub-national scales.

Landsat-based basin-wide mapping of crop water use, without merging with other satellite data, has been conducted for the Colorado River Basin (Singh et al., 2014; Senay et al., 2016) by processing up to 528 images to produce annual ETa using the Operational Simplified Surface Energy Balance (SSEBop) model (Senay et al., 2013; Senay, 2018). Historical application of the SSEBop model has shown the consistency of the model for water use trend analysis in addition to providing field-scale ETa over southern California (Senay et al., 2017)

and Upper Rio Grande Basin (Senay et al., 2019). One of the main challenges for historical analysis of Landsat-based ETa was the computational resources required to process a large number of images to create annual ETa. For example, 3396 Landsat images were processed to create 31 years (1984–2014) of annual ETa for southern California and 10,335 images were used for generating 32 (1986–2015) years of annual ETa for the Upper Rio Grande Basin studies. The first attempt to apply the SSEBop model historically in Google Earth Engine (GEE) was a 10-year study of the Central Valley of California for analyzing crop water use (Schauer and Senay, 2019). These historical studies demonstrated the capability and stability of the SSEBop model to capture the spatiotemporal dynamics of complex basins, indicating the possibility to conduct Landsat-scale ETa for the entire conterminous United States (CONUS) and for the world as long as Landsat data and accompanying weather variables are available and computational limitations are overcome. More recently, the capability of GEE for implementing several ETa models is summarized by the OpenET initiative (Melton et al., 2021).

To illustrate the capabilities of Landsat-based ETa estimates over large areas, we present a CONUS-wide study by implementing the SSEBop model on the GEE cloud computing platform. The GEE SSEBop implementation solves the major computing challenges in creating continental scale ETa by eliminating the user's need for large data storage and reducing the time it takes to process and conduct ETa calculations from months to days. The main objectives of this study are as follows: (1) create 10 years (2010–2019) of Landsat-scale annual ETa for CONUS, (2) describe GEE-enabled model parameter improvements and cloud implementations, (3) evaluate SSEBop model performance using EC and basin Water Balance ETa (WBET) methods, and (4) demonstrate application examples using ETa anomalies for drought monitoring and fire impact assessment.

2. Methodology

2.1. SSEBop model description

The SSEBop model estimates landscape ETa directly using a satellite psychrometric principle (Senay, 2018). Using a two-step procedure, an ET fraction (ETf, defined as the ratio of actual to reference ET) is first calculated as a difference between the observed land surface temperature (dry bulb) and a wet-bulb reference surface temperature as shown in Eq. (1).

$$ETf = 1 - \gamma^s(Ts - Tc) \tag{1}$$

where *ETf* is the daily ET fraction (0.0–1.0) for each pixel; γ^s is the surface psychrometric constant (1/K) over a dry-bare surface and is the same as the inverse of the *dT* (temperature difference, K) parameter in Senay et al. (2013); *Ts* is the dry-bulb surface temperature (K) derived from the Landsat thermal band, and *Tc* is the wet-bulb reference surface temperature (K) limit, derived from *Ta* (daily maximum air temperature). The constant 1 represents the ET fraction value during maximum ETa, i.e., when $Ts = Tc$.

Daily ETa is then determined on a per-pixel basis using Eq. (2):

$$ETa = ETf * ETr \tag{2}$$

where *ETa* is actual ET (mm), *ETr* is alfalfa-reference ("potential") ET (mm).

Here we use the GridMET dataset (Abatzoglou, 2013) for ETr. However, GridMET has been reported by Blankenau et al. (2020) to overestimate ETr, with biases ranging from 12 to 31% across CONUS. Thus, a constant bias correction of 0.85 was applied in this study (Bawa et al., 2020). During drought years, anomalously large values of ETr can occur, exaggerating the actual ET even when the ET fraction is small. A typical example of this occurred during a drought year in 2012. A location near Peoria Illinois (−89.7226E, 40.6510 N) registered a GridMET ETr of 22.95 mm/day on June 28th while the 1980–2017

climatological median for that day of year was only 6.77 mm/day according to the Climate Engine web application tool (https://app. climateengine.com; Huntington et al., 2017) with the year total exceeding the median year by more than 40%. To generate ETa in this analysis, a climatology (daily median of 1980–2017) ETr was used for the entire period of study. This helps to reduce anomalously high ETr values during drought years (Senay et al., 2013) and enables the surface temperature (from Landsat) component to guide the SSEBop model to respond to surface agronomic conditions, i.e., year-to-year ETa variations are dependent on ETf rather than ETo.

For time integration, SSEBop monthly and annual ETa aggregation included linear interpolation of ETf on a daily timestep for days between Landsat satellite overpass images. ETf values are then multiplied by daily ETr to produce daily total ETa for every pixel followed by summation to monthly or annual time periods. Detailed information on GEE implementation of the processing and data management is presented in Section 2.2.

In this study, the following changes have been implemented regarding the two model parameters in Eq. (1): (1) γ^s was determined using a gray-sky radiation instead of clear-sky assumptions, and (2) the wet-bulb Tc was estimated using a gridded c factor approach instead of a scene wide mean value.

2.1.1. Gray-sky dT ($1/\gamma^s$)

The surface psychrometric constant γ^s was estimated as the inverse of dT from a gray-sky radiation source as opposed to clear-sky assumptions applied in previous studies. The gray-sky was chosen because the clear-sky gives a more unform and unrealistically high net radiation (high dT) in much of the world while the gray-sky net radiation is based on observations that account for localized prevailing atmospheric conditions such as haze and water vapor to produce a reasonable dT. Gray-sky dT was determined from observed radiation sources provided by the European Center for Medium -Range Weather Forecasts (ECMWF) Reanalysis (ERA) climate dataset at 10-km resolution (https://cds.climate. copernicus.eu/cdsapp#!/dataset/reanalysis-era5-land), resulting in an improved spatial representation of the net radiation parameter. A 30-m Digital Elevation Model (DEM) data allowed the creation of a 1 km resolution dT product from 10-km radiation data through the air density parameter in Eq. (3).

$$\gamma^s = \frac{\rho * C_p}{R_n * r_{ah}} \tag{3}$$

where ρ is the density of air (kg.m^{-3}), calculated as a function of elevation (Allen et al., 1998; Senay et al., 2013); C_p is specific heat of air at constant pressure, 1.013×10^{-3} (MJ·kg^{-1}·$^\circ$C^{-1}); R_n is the daily average net radiation (MJ·m^{-2}·d^{-1}); and r_{ah} (s·m^{-1}) is the aerodynamic resistance over dry-bare soil (Senay et al., 2013).

The aerodynamic resistance was determined to be 165 s·m^{-1} in this study, compared to 110 s·m^{-1} in previous studies, due to a change in the source of radiation from clear-sky to gray-sky. The recalibration was done using observed dT (not presented), which was determined from manually identified hot/bare-dry and cold/vegetated-wet pixels in irrigated fields across different parts of the western United States. The R_n was estimated using the following equation:

$$R_n = 0.5 * (R_{ns} - R_{nl}) \tag{4}$$

where R_{ns} is the net shortwave radiation calculated using surface albedo (α) = 0.23, i.e., R_{ns} = (1- α)* R_s; R_s is the daily maximum downward shortwave radiation from the ERA5-Land dataset.

The daily average was assumed to be the average of early morning (R_{ns} = 0) and daily maximum, thus the use of the 0.5 coefficient. Ten years (2001−2010) of daily ERA5-Land data were used to select the 90th percentile, representing the "cloud-free" condition for remote sensing ETa without including a potential outlier (9th highest of 10 years). It is important to note that the R_n is not a direct model driver, but an input

parameter to set a maximum boundary condition for the expected radiation input over a dry-bare soil that would give a maximum dT. The daily maximum R_{nl} was found to only constitute a small fraction (<2%) of the daily maximum R_{ns}; thus, we chose not to include it in the final Rn calculation, i.e., R_{nl} = 0.0. Because the dT was to be calibrated using the r_{ah} parameter as described above, the 2% contribution of the R_{nl} would not make a meaningful difference to the final dT as it is a calibrated parameter. A 10-day moving average was used to smooth the R_n in order to create R_n that would be experienced during a satellite-overpass on a typical cloud-free day. Similarly, the use of a constant albedo of 0.23 for the bare soil is based on a reasonable approximation, but using a different value would be countered by a change in the r_{ah} magnitude without affecting the final dT through the calibration process (Senay et al., 2013).

2.1.2. Gridded c factor

The ability to recognize spatiotemporal association of model parameters (Table 1) through big data processing and new evaluation enabled us to implement an improved approach for nationwide Landsat ET modeling that handles more complex parameter interactions.

The c factor allows the conversion of a gridded daily maximum air temperature (Ta) into a wet-bulb (Tc) parameter in Eq. (1) (Senay et al., 2013, 2017). Senay et al. (2017) showed the importance of a temporally dynamic c factor by determining a unique c for each day of satellite overpass. In this study, a spatially dynamic c factor (gridded c) was developed at 5-km resolution to overcome assumption failures over complex terrain in the applicability of a single scene-wide c factor.

To illustrate this, an initial CONUS-wide implementation of the GEE-based SSEBop revealed irregular model patterns (artifacts) in parts of the western United States such as the Salinas Valley in California (Fig. 1). The main finding was that air and land surface temperature relation over well-watered surfaces do not necessarily behave uniformly over large distances across a Landsat scene. This finding revealed the drawback of using a scene-reduced single c factor (Eq. (5)) for modeling the entire Landsat scene. With the computing capabilities of GEE to enable these data driven insights, we were able to introduce a gridded c factor that handled the unique spatial association between Ts_cold and Ta over complex topographic regions.

$$c = \frac{Ts\_cold}{Ta} \tag{5}$$

where Ts_cold (K) is the land surface temperature at the cold/wet-vegetated surface; Ta (K) is the daily maximum air temperature over the Ts_cold pixel that is defined as areas with high density green vegetation with a Normalized Difference Vegetation Index (NDVI) ≥ 0.7 and representing the coldest 2.5 percentile (Senay et al., 2017).

Once the c factor is determined for a given modeling space based on Eq. 5, the cold/wet reference boundary condition (Tc) is calculated using Eq. (6).

$$Tc = c * Ta \tag{6}$$

where c is the correction factor that converts Ta over a given pixel to its Tc equivalent.

Cold/wet pixel selection was accomplished by selecting Ts_cold (~100 m) values from high NDVI pixels (~30 m) that were focally

Table 1
SSEBop model input, parameter list, and data sources.

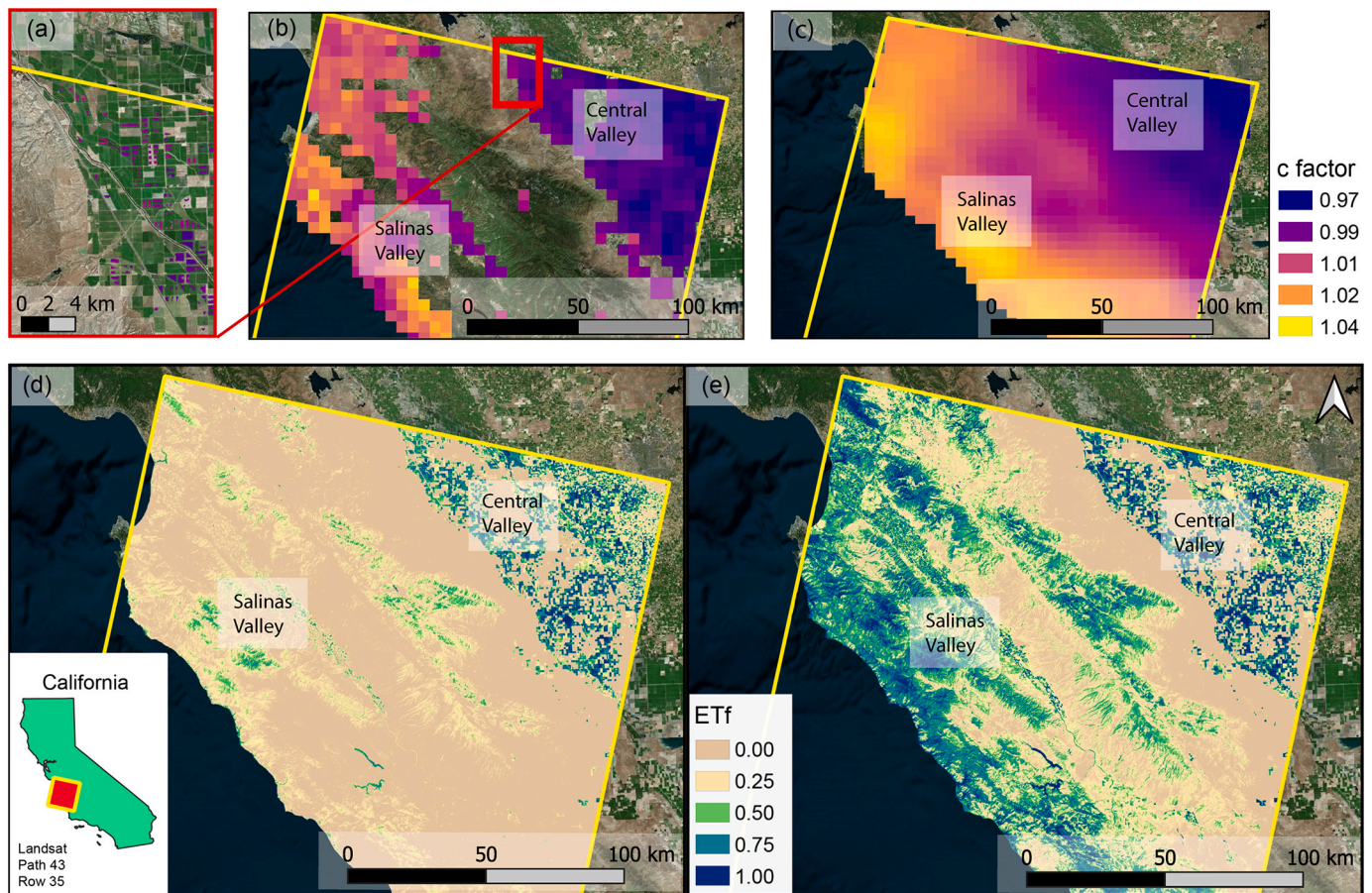| Input	Parameter	Source
Surface Temperature	Ts, Ts_cold	Landsat
Vegetation Index	NDVI: filter Ts_cold	Landsat
Maximum Air Temperature	Ta, Tc	Daymet
Elevation (DEM)	DEM: air density, dT	SRTM
Reference ET	ETr	GridMET
Net Radiation (Rn)	dT ($1/\gamma^s$)	ERA5-Land

Fig. 1. Maps summarizing the process of computing gridded *c* for a given Landsat overpass (July 15, 2019) and demonstrating the effect on ETf using an improved algorithm. Inset on bottom left shows a location map with the Landsat path/row boundary in yellow outline over the Salinas Valley and Central Valley, California. (a) 30-m resolution *c* factor on individual high NDVI pixels as the basis for the (Ts_cold/Ta) calculation; (b) The *c* factor is upscaled to a 5-km grid cell by using the 2.5th percentile value within the 5-km grid cell; (c) Focal averages create a smooth gridded *c* factor over the entire scene; (d) ETf that results from previous method using a single scene-wide *c* factor; (e) ETf using an improved gridded *c* factor algorithm. (For interpretation of the references to colour in this figure legend, the reader is referred to the web version of this article.)

smoothed (mean 90-m radius). This ensured *Ts_cold* was minimally affected by thermal edge boundaries that occur in areas where high NDVI pixels are surrounded by dry surfaces (Fig. 1a).

An individual *c* factor value was calculated for every 5-km grid cell across each Landsat scene. Where base selection conditions are not met (i.e., NDVI <0.7), focal average fill techniques using subsequent larger kernels (3 × 3, 5 × 5, etc.) were used to generate complete scene coverage with a gradually varying *c* factor surface for each day of overpass at 5-km resolution (Fig. 1b, c). To reduce algorithm complexity, adjoining Landsat images within the same path were not used to calculate *c* factor. Roughly 7% of total Landsat scenes used in this study (not presented) did not meet *c* factor criteria, primarily occurring in winter months during the non-growing season. Further analysis to explore these effects and operational solutions for parameterization at sub-annual scales and non-growing seasons would be beneficial. Each gridded *c* factor image was precomputed and kept as an image collection model asset with preserved Landsat image ID and source-quality information for data provenance and efficient use within the SSEBop ETa processing steps.

The gridded *c* factor approach shows reasonable distribution of ETf compared to the previous single *c* factor implementation (Fig. 1e versus 1d) where the irrigated Salinas Valley and adjoining forested areas exhibit higher ETf (up to 1.0, Fig. 1e) that was vastly underestimated in Fig. 1d (less than 0.5 ETf in most places). Both methods produced similar ETf over the northeast areas of the image (Central Valley), indicating the

scene-wide *c* factor was dominated by the large number of high NDVI pixels in the Central Valley, reasonably modeling this area but not in Salinas Valley. This is primarily due to *Ta* being cooler in relation to *Ts* in the Salinas Valley as compared to over the Central Valley.

2.2. Cloud computing

Cloud computing has specifically transformed the ways we are able to think about SSEBop ETa modeling in relation to data volume, collaborative insights, and spatiotemporal scales. The GEE parallel cloud processing platform (Gorelick et al., 2017) enabled us to focus on functionality for process improvements and results assessments of SSEBop ETa at a nationwide scale for the first time. Access to extensive volumes of remote sensing and related geospatial data in a centralized system next to dedicated computing infrastructure dramatically reduces satellite ET modeling hurdles such as data acquisition, storage, and parsing database files, thereby reducing project time and costs. Furthermore, connecting to and sharing code or data assets is not limited by things such as access controls, system setup, or network permissions but is intuitive and illustrative for faster big data science iteration and facilitating extensible collaboration benefits which are more readily realized with cloud-hosted data analysis strategies. Using built-in geospatial Application Program Interfaces (APIs), model methods are optimized for imagery-cloud mitigation, time integration, and quality information, with an overarching goal to generate 30-m resolution scale

ETa maps for the entire Landsat archive. The following sections detail the procedures for implementing the SSEBop model on the cloud and techniques used for model performance evaluation.

2.2.1. Cloud implementation

We developed a complete SSEBop ETa modeling framework on the GEE platform using the Earth Engine Python API. An overview of the cloud implementation schematic is shown in Fig. 2. Development of the model in this way enabled the use of automated raster handling functions over all utilized image collections for processing scene-wide ET fraction, linear interpolation of daily ETf, creating daily ETa, and aggregation to annual ETa for all of CONUS. Specifically, client library operators provided by the Earth Engine API are natively built for implementation as a *map-reduce* style of programming model, where a set of developed pixel-based "band math" functions or other geospatial methods can be applied to a large time series of spatially filtered or joined image collections. Here, we leveraged the parallel processing and distribution framework of the GEE system architecture (detailed in Gorelick et al., 2017) for connecting key SSEBop model functions and algorithms (Section 2.1) together when generating both intermediate results and aggregated ET products.

Model setup and configuration for SSEBop utilized public data catalog inputs such as Landsat and meteorological data as described in Section 2.2.2. The unique nature of Earth Engine's co-located data and parallel computing resources facilitated the ability to affordably iterate on scientific investigation efforts for new data insights and improvements in model parameters such as with weather datasets or gridded *c* factor, while also building repeatable, operational capabilities.

Cloud processing enables SSEBop to model 30-m ETa data over large areas without traditional desktop hardware limitations. More than 150,000 Landsat scenes were processed for the years 2010–2019 across CONUS, an evolutionary step forward for ETa modeling of moderate-resolution Landsat data.

With the advanced capabilities of Earth Engine, Landsat-based ET operations are scalable to continental or global applications. For example, GEE computation services use load-balancing distribution software for parallel pipeline execution of per-image requests, which allows SSEBop to use all available Landsat pixels synchronously in data- and memory-intensive functions for interpolation using temporal gap-filling procedures as described in Section 2.1. The accessibility of centralized datasets and processing for meaningful geospatial analysis is supportive to a wide variety of integrative science activities and strategies well into the future.

2.2.2. Data catalogs

On-demand centralized access to the full Landsat archive as well as other climate and weather datasets needed for ETa modeling eliminated the need to download and store terabytes of raw data or repeatedly manage intermediate outputs. We used Landsat Collection 1 Tier 1 imagery from the GEE data catalog (https://developers.google.com/earth-engine/datasets) to obtain Cloud Masks using the CF-Mask derived Landsat QA band, NDVI, and *Ts* (via a retrieval method from Senay et al., 2016). We filtered our initial image collection to those with less than 60% cloud cover to remove excessively clouded and cloud-contaminated Landsat scenes yet retain adequate image counts for each pixel in our calculations. Particularly, scene-path overlap areas provided upwards of 50+ unique observation dates a year in many locations when using two Landsat sensors (Thematic Mapper (TM) & Enhanced Thematic Mapper (ETM+) or ETM+ & Thermal Infrared Sensor (TIRS)) for gap-filling and time integration procedures. See section 3.1 for more image count information.

Other ancillary datasets for SSEBop modeling included a climatological average (1980–2018) daily maximum air temperature (*Ta*, 1 km) from Daymet (Thornton et al., 2016); a digital elevation model (DEM, 30-m) dataset from the Shuttle Radar Topography Mission (SRTM) (Farr et al., 2007); climatological median (1980–2017) daily alfalfa-based Reference ET (ETr, 4-km) from GridMET (Abatzoglou, 2013), and surface psychrometric constant (γ^s, 1 km) estimated from a gray-sky radiation source ERA5-Land dataset (https://cds.climate.copernicus.eu/cdsapp#!/dataset/reanalysis-era5-land, 10-km). These input image collections are accessible in the GEE data catalog.

2.3. Model performance evaluation

Quantitative model performance was evaluated using EC ETa data at point scale and annual Water Balance ETa at Hydrologic Unit Code (HUC) level 8. Data from more than 25 EC towers and up to 1104 HUC-8 s were used.

2.3.1. Eddy covariance (EC) evaluation

Following prior studies as in Senay et al. (2019), the accuracy of the SSEBop ETa results was evaluated with aggregated monthly ETa from EC data derived from the AmeriFlux network (https://ameriflux.lbl.gov/) for 2005–2014. Due to biases inherent in processing choices for gap-
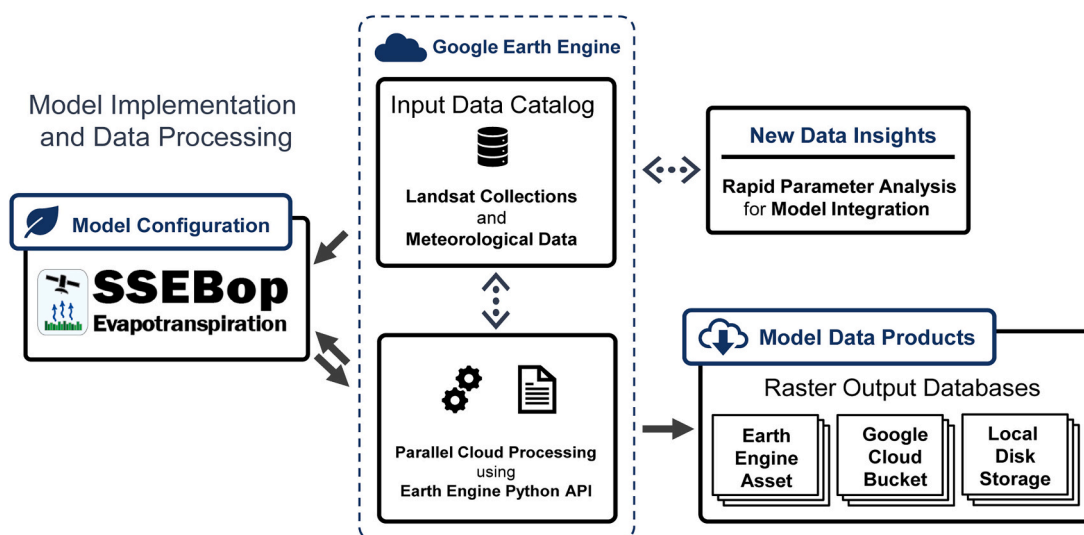

Fig. 2. Overview of SSEBop Landsat model framework in the Google Earth Engine cloud platform. Senay et al. (2016) shows the SSEBop model portion of the flow chart in more detail.

filling and energy balance closure, we chose to utilize the FLUXNET2015 data product, which quantifies and standardizes gap-filling and energy balance closure with a uniform method to improve the consistency across sites for intercomparisons (Pastorello et al., 2020). The FLUX-NET2015 product comes with the energy balance closure already completed, described in detail by Pastorello et al. (2020). In brief, the energy balance closure is based on the Bowen ratio and by correcting the latent heat (LE) and sensible heat (H) by an energy balance closure correction factor (EBC_CF) using a sliding window methodology on the original half-hourly flux tower data. FLUXNET2015 data were chosen for 25 sites across CONUS from 2005 to 2014 and were filtered to exclude days with high energy balance closure error of more than 20%. The daily average of the corrected, gap-filled LE turbulent flux in W/m^2 was then converted to daily ETa in mm/day using a conversion factor of 0.03525 based on the LE of vaporization (Senay, 2008). Monthly ETa from each tower location was only aggregated when at least 26 days of daily ETa could be calculated.

The final selection of FLUXNET2015 sites includes a mix of landcover types such as cropland, forests, shrublands, and grasslands, but the sites are spatially located primarily in the western and midwestern states (Fig. 3). The east coast and southern states are poorly represented by EC towers. Monthly SSEBop ETa was calculated using the same GEE techniques noted above for areas covering the FLUXNET2015 site locations from January 2005 to December 2014. In order to standardize sampling and compensate for temporally varying source area footprints around each tower location, a spatially averaged ETa was sampled for a 45-m circular buffer around each tower location for every month. Coefficient of determination (R^2), bias, and root mean square error (RMSE) values were computed to quantify statistical agreement between the SSEBop ETa and FLUXNET ETa.

2.3.2. Water balance evaluation

Water Balance ETa at HUC8 sub-basins was compared with SSEBop ETa at the water-year (October 1 – September 30) timestep. The water-year scale minimizes the effect of unaccounted storage changes that are important at shorter time scales. The water-year (hereafter named as annual) WBET for HUC8s was computed as:

$$WBET = P - Q - \Delta S \tag{5}$$

where, P, Q, and ΔS are annual precipitation, runoff, and storage change at HUC8 sub-basins, respectively.

An independent ETa dataset was generated from the water balance approach at the HUC8 scale to compare with ETa estimations from the SSEBop model. The CONUS is divided into hydrological unit systems identified by a unique HUC consisting of two to eight digits for representing the geographic areas (Seaber et al., 1987). The largest geographic area is a region identified by a unique HUC2 number, followed by sub-region (HUC4), basin (HUC6), and sub-basin (HUC8). The HUC8s within the CONUS were considered in this study with a total number of 2121 HUC8s (Fig. 3). The sizes of these HUC8 sub-basins are between 184 km^2 and 84,706 km^2 with an average of 4027 km^2.

For the Water Balance ETa (WBET) estimation at the HUC8 scale, precipitation and runoff data were used. In this study, we used the monthly precipitation data at 4-km spatial resolution, obtained from the Parameter-elevation Regressions on Independent Slopes Model (PRISM) (Daly et al., 1994), which are publicly available at the Oregon State University PRISM Climate Group website http://www.prism.oregonstate.edu/.

The runoff data for HUC8s were obtained from the U.S. Geological Survey (USGS) WaterWatch website (https://waterwatch.usgs.gov/). We used the annual runoff data that are available as a single value (non-spatial) for HUC8s. These runoff data are generated from historical flow observations at the USGS stream gages, drainage basin boundaries of the stream gages, and the HUC8 boundaries (Brakebill et al., 2011). Previous studies (Senay et al., 2011; Velpuri et al., 2013; Senay et al., 2016) have applied the PRISM precipitation and the USGS WaterWatch runoff data for computing ET from the water balance approach to compare with the ETa estimated from the SSEBop model.

Monthly P and Q were aggregated to annual totals to obtain a single basin-average value for each HUC8. The annual storage change (ΔS) was assumed to be negligible (0.0) during the study period.

Following similar assumptions and techniques reported in the literature, several filters were applied to exclude HUC8s where the water balance is not expected to close (WBET $\neq P - Q$) due to several factors: For example, for the mean year, HUCs along the boundary of the CONUS (176 HUC8s) were excluded due to incomplete precipitation data, HUCs with runoff (Q) to precipitation ratio (Q/P) > 0.40 (364 HUC8s) were excluded to reduce effects of regional groundwater flow (e.g. Velpuri et al., 2013; Senay et al., 2016), and HUC8s with WBET greater than potential ET (8 HUC8s). Additionally, HUCs with SSEBop ETa greater than precipitation (540 HUC8s) were excluded for unrealistic ETa and heavily irrigated HUCs that the WBET does not take into account. After these filters (2121-176 - 364 - 8 - 540) and adding 30 HUCs for double
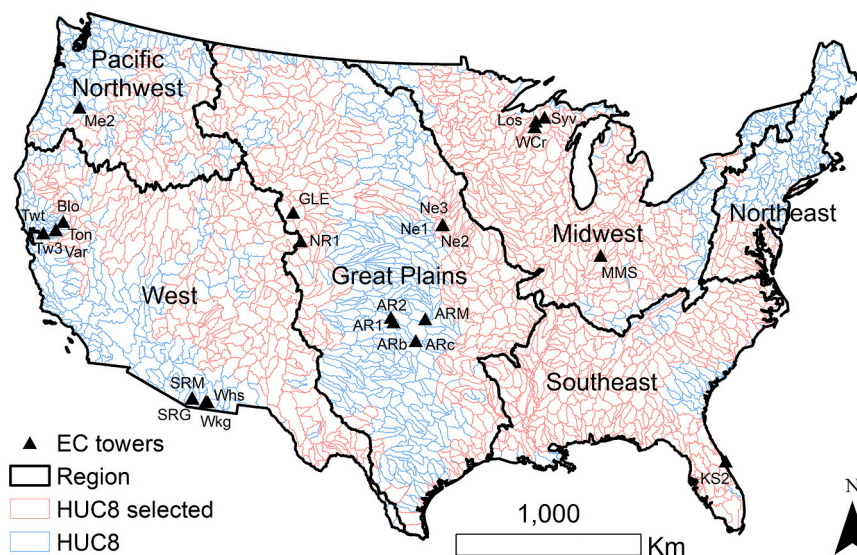

Fig. 3. Location of eddy covariance (EC) towers used in this study, selected eight-digit Hydrological Unit Code (HUC8) boundaries (red) and the six regions of the conterminous United States. (For interpretation of the references to colour in this figure legend, the reader is referred to the web version of this article.)

accounting from multiple criteria, 1063 HUC8s (50% of 2121 HUC8s across the CONUS) were selected for the evaluation.

The annual total ETa from SSEBop was compared with WBET for average and individual years during the 10-year (2009–2018 water-year) period. The water-year period for 2009/2018 refers to the October 1, 2008/2017 through September 30, 2009/2018 time periods.

The ETa comparisons were grouped across six different hydro-climatic regions of the CONUS (Fig. 3) to evaluate the performance of SSEBop across the regions. R^2, bias, and RMSE were applied for statistical analysis.
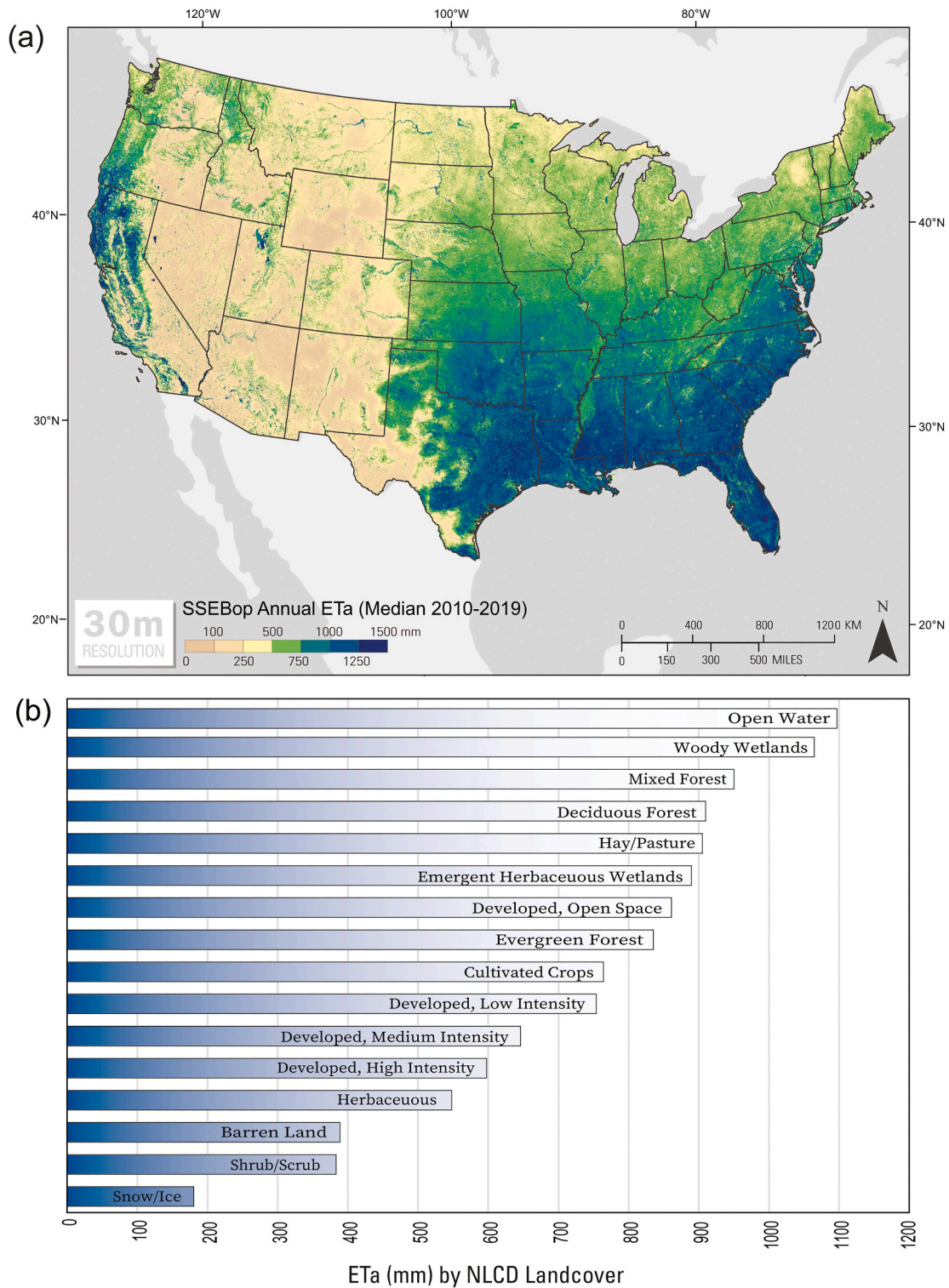

Fig. 4. SSEBop median annual (January–December) ETa (mm) from 2010 to 2019 across the conterminous United States at 30-m resolution (a). CONUS-wide spatial averages of median annual ETa by NLCD landcover (b). Gridded data are available at https://doi.org/10.5066/P9SJLMAQ (Senay et al., 2021b).

3. Results and discussion

3.1. Model outputs and cloud-free image analysis

One of the main objectives of this study was to demonstrate the successful implementation of the SSEBop model with GEE. Gridded outputs included Landsat-resolution 10-year annual ETa (2010–2019) (Senay et al., 2021a, 2021b) and cloud-free pixel count quality information. It should be noted that the integration of cloud-free image masks was determined from the Landsat QA band for the "clear, high-confidence" classification, which included masking of clouds, shadow, snow, and ice. Therefore "cloud-free pixel count" refers to usable image
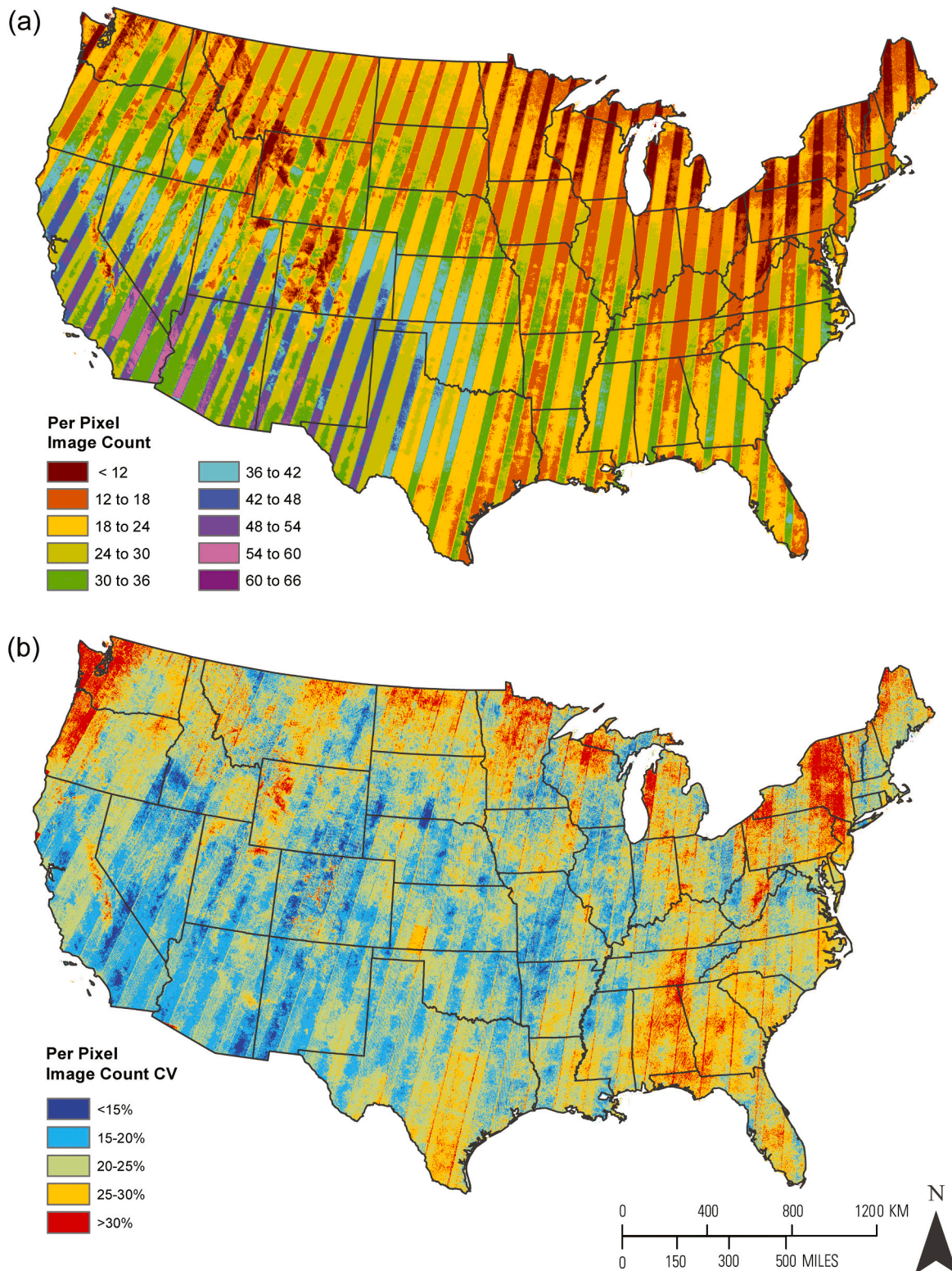

Fig. 5. Ten-year (2010–2019, January–December) mean annual clear-image pixel count for CONUS (a) and coefficient of variation (CV) per-pixel (b). Cloud-affected regions show with lower counts and regions with a high year-to-year variability show with a high CV. Data were resampled to 250-m resolution for display.

observations based on those designations on a per-pixel basis. Earlier studies suggest a minimum of 12 cloud-free images for a given pixel, distributed uniformly each year, are necessary for a reasonable estimation of annual ETa (e.g., Singh et al., 2014).

The generation of annual median ETa required more than 150,000 Landsat images (~15,000 per year) in addition to gridded weather data layers. The median annual ETa distribution (Fig. 4) shows the obvious high and low ETa magnitudes over well-vegetated and barren surfaces, respectively (Senay et al., 2021a). Using the National Land Cover Database (NLCD) by Homer et al. (2015), nationwide landcover-type spatial averages for open water and woody wetlands were estimated to experience $ETa > 1000$ mm/year with croplands showing a range of 700–800 mm/year and barren lands having <400 mm/year (Fig. 4b).

The high ETa values in the western United States are mainly concentrated over irrigated areas such as the Central Valley in California, Snake River Basin in Idaho, and Columbia Plateau in Washington. Despite the general depiction of high and low ETa areas according to the expected land cover and hydro-climatic regions, unexpected artifacts of ETa are observed in different parts of CONUS such as central Texas and northeastern New York. Some of these artifacts can be attributed to availability of cloud-free images. Especially, the low ETa region in northeast New York coincides with the low image count and high coefficient of variability shown in Fig. 5a and b, respectively.

The ability to produce consistent and accurate estimates of monthly and annual ETa products depends in part on meeting an adequate clear pixel count and an interannual consistency in pixel count. Fig. 5 shows a general decreasing clear-image pixel count (annual mean) from southwest to northeast CONUS, ranging from >60 (Arizona) to <12 (Maine). Fewer clear-image pixel counts are also observed in the northwest and over the Rocky Mountain Range. The relatively large range of coefficient of variation in CONUS indicates the importance of conducting a careful quality assessment to make sure minimum image counts are met. It should be noted that the contrasting high-low image count patterns, a result of more frequent images on overlapping path/rows, did not seem to influence the annual ET patterns in Fig. 4, indicating a reasonable number of clear images were available each year to create the annual estimate across CONUS. But it is important to note that these differences in image count on overlapping path/rows could bring a marked difference in the monthly estimates, especially in cloud affected regions.

Table 2 shows the top and bottom-ranked states based on number of clear-image pixel counts by calendar year. The top-ranked states with the greatest number of clear images (Arizona, California, New Mexico, Nevada, Utah) benefit from over twice as many (~38 versus ~14) median images per year relative to the bottom five states (Vermont, Maine, New York, Michigan, Pennsylvania). A median number of 14 images per

Table 2
Cloud-free image pixel count summary statistics for the top and bottom states ranked by median count. Ten year (2010–2019, January–December) clear-image pixel count (median, mean, minimum (min), and maximum (max)) were averaged for each state. Range, Standard Deviation (STD) and Coefficient of Variation (CV) were calculated from the state-wide summaries.

State Name	Median	Mean	Min	Max	Range	STD	CV(%)
Top Five States							
Arizona	38.0	36.4	18.2	44.6	26.4	7.2	19.8
California	36.3	34.7	17.1	42.7	25.6	7.0	20.3
New Mexico	35.3	34.0	18.3	42.6	24.3	6.8	19.9
Nevada	31.6	30.6	15.8	38.3	22.5	6.1	19.9
Utah	29.2	28.4	15.5	36.5	21.0	5.9	21.0
Bottom Five States							
Pennsylvania	16.2	16.0	8.5	22.8	14.3	4.3	27.0
Michigan	15.4	15.4	8.6	22.1	13.5	3.9	25.9
New York	15.1	15.3	8.0	24.2	16.2	4.6	30.5
Maine	15.0	14.8	8.0	20.8	12.8	3.8	26.5
Vermont	14.2	14.5	8.7	22.0	13.4	3.8	26.0

year might be too close to the ideal minimum (12), especially when considering a non-uniform distribution of images to obtain a reliable estimate for each month. The bottom-ranked states also occur mostly in the Northeast region of the United States. This region lacks representative EC tower data and has the lowest number of samples of WBET (see sections 3.2 and 3.3). In terms of uncertainty regarding annual total ET estimation, the Northeast United States is a particularly challenging region. Of note, the mapping analysis of both ETa and clouds presented here at CONUS scale is showing annual summaries over the 10-year period of study. Therefore, future research and investigation into subannual timeframes would be helpful to aid in understanding these regional effects in more detail.

In addition to image quality and availability, the sources of ETa error could range from other model inputs to model parameters as discussed in Section 3.5. Although it is difficult to thoroughly evaluate the accuracy of the product in all extents of the study area, the point-based EC and WBET shown below can provide some information on the behavior of the model performance at different scales and regions.

3.2. Performance against EC towers

Validation results of monthly SSEBop ETa based on the data from 25 EC sites for all available years are presented in Table 3 and Fig. 6. Although the FLUXNET2015 dataset has already undergone through an energy balance closure correction, there remains an average closure error of around 4% (ranges 3–6%). However, this error does not correlate with the percent bias of the SSEBop ETa against ETa from EC towers. The R^2 varied substantially by EC tower site (R^2 ranged from 0.35 to 0.95) with an average of 0.68 over all cover types. The average RMSE for all sites was 32 mm/month. SSEBop overestimated the FLUXNET ET by an average percent bias of 30% for all EC sites. Most sites (20 out of 25) had positive bias values that ranged from 2% to 98%, indicating a general overestimation of SSEBop ETa compared to observed ETa from the EC towers. At five EC towers, SSEBop underestimated ETa by an average of 27%.

Validation results by land cover showed that the performance of SSEBop ETa appears to vary with land cover types (Table 3). SSEBop performed best on cropland sites. The average of the six cropland sites shows a strong R^2 value of 0.82 and a relatively lower bias (12%) and an average RMSE of 29 mm/month indicating that SSEBop model performed more accurately in agricultural areas (Table 3). The pooled data analysis for croplands shows similar results with an R^2 of 0.80, bias of 9%, and RMSE of 30 mm/month (Fig. 6). While the pooled dataset (Fig. 6) for the seven forested and the seven grassland sites show that SSEBop overestimated the EC data by 28% and 45%, respectively, site averages from Table 3 show an average bias of 39% and 45%, respectively, indicating a larger bias difference between pooled (Fig. 6) and site averages (Table 3) for the forest sites. Forested sites (average of 7 sites, Table 3) show an average determination R^2 of 0.70 and average RMSE of 34 mm/month while grassland sites show an average R^2 of 0.61 and average RMSE of 36 mm, indicating SSEBop is still moderately correlated with both forest and grassland landcover sites but with higher bias in magnitude and higher error. The site averages (Table 3) tend to show improved R^2 compared to pooled (Fig. 6) data because of the effect of averaging in reducing random errors. Although there are only two shrubland sites, SSEBop performed reasonably with an average R^2 of 0.59 and average RMSE of 21 mm with a − 12% bias (Table 3). SSEBop showed mixed performance on the two woody savanna sites with an average R^2 of 0.57, RMSE of 30 mm, and a 20% bias. In comparison, the one wetland site (US-Los in Wisconsin) also shows a substantial overestimation of 73% for SSEBop over the EC tower, but higher R^2 of 0.77 and lower error with an RMSE of 29 mm, indicating that SSEBop captured the seasonal variability of the tower but overestimated the magnitude for the wetland site. The large overestimation over this wetland site warrants further investigation of the EC tower site in case there is a strong spatial mismatch using EC tower footprint analysis

Table 3

Statistical comparison between FLUXNET2015 observations from 25 Ameriflux EC flux towers and monthly total ETa estimates from SSEBop during 2005–2014. The table includes the average monthly EC ETa, average monthly SSEBop Landsat ETa for the tower, U.S. state abbreviation, NLCD landcover type Homer et al. (2015), average difference (bias) in monthly ETa, R^2, RMSE, and the percent bias of SSEBop compared to average FLUXNET monthly ETa. Average energy balance closure error is also included (%). Accuracy metrics are also summarized by cover type as site averages.

Site	State[*]	Land cover	EC (mm)	SSEBop (mm)	Bias (mm)	Energy Balance Closure Error (%)	R^2	RMSE (mm)	Bias (%)
US-ARM	OK	Cropland	48	72	24	5	0.65	37	50
US-Ne1	NE	Cropland	74	68	−9	4	0.79	31	−8
US-Ne2	NE	Cropland	67	69	−4	4	0.83	27	3
US-Ne3	NE	Cropland	57	61	−1	4	0.83	23	7
US-Tw3	CA	Cropland	91	94	3	3	0.87	26	3
US-Twt	CA	Cropland	115	136	21	4	0.94	31	18
Average of All Cropland Sites							0.82	29	12
US-Blo	CA	Forest	59	92	33	5	0.77	39	56
US-GLE	WY	Forest	56	67	2	6	0.52	34	20
US-Me2	OR	Forest	53	76	23	5	0.58	36	43
US-MMS	IN	Forest	55	77	22	5	0.85	31	40
US-NR1	CO	Forest	61	53	−18	5	0.70	29	−13
US-Syv	MI	Forest	50	66	15	6	0.85	26	32
US-WCr	WI	Forest	46	91	31	6	0.64	41	98
Average of All Forest Sites							0.70	34	39
US-AR1	OK	Grassland	39	69	30	5	0.35	46	77
US-Arb	OK	Grassland	65	104	39	3	0.89	45	60
US-Arc	OK	Grassland	67	103	36	2	0.95	39	54
US-SRG	AZ	Grassland	38	16	−24	3	0.65	33	−58
US-Var	CA	Grassland	30	48	18	4	0.54	32	60
US-Wkg	AZ	Grassland	24	35	11	4	0.50	23	46
US-AR2	OK	Grassland	32	56	24	5	0.36	37	75
Average of All Grassland Sites							0.61	36	45
US-SRM	AZ	Savanna	30	20	−11	3	0.53	23	−33
US-Ton	CA	Savanna	39	67	29	4	0.60	37	72
Average of All Savanna Sites							0.57	30	20
US-KS2	FL	Shrubland	96	98	1	4	0.60	24	2
US-Whs	AZ	Shrubland	24	18	−7	3	0.57	18	−25
Average of All Shrubland Sites							0.59	21	−12
US-Los	WI	Wetland	45	78	20	6	0.77	29	73

[*] AZ: California; CA: California; FL: Florida; IN: Indiana: MI: Michigan; NE: Nebraska; OK: Oklahoma; OR: Oregon; WI: Wisconsin; WY: Wyoming.
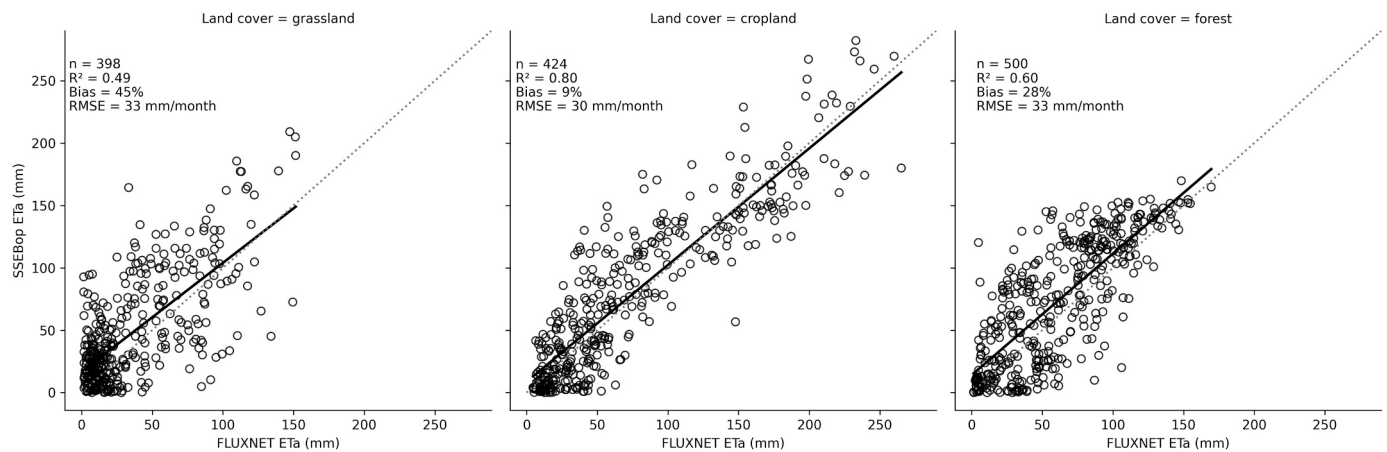

Fig. 6. Scatterplots of monthly ETa values for grassland ($n = 7$), cropland ($n = 6$), and forest ($n = 7$) sites from FLUXNET eddy covariance towers compared against the Landsat SSEBop ETa for the tower locations. The gray line is the 1:1 and the solid dark line is the best fit with "n" representing the number of months in each landcover group during 2005–2014.

considering the 45 mm/month (540 mm/year) ET for a wetland site is on the low side.

Fig. 7 also demonstrates similarity in NDVI and ETa seasonal patterns and their inter-annual variability. It can be observed that SSEBop tends to be a smoother curve compared to the EC data. For example, SSEBop missed the sudden dip during the summer of 2009 for US-MMS (broadleaf forest), which may be tied to using a climatology ETr. It was reassuring that both SSEBop and EC data captured the narrow growing season at US-Ne3, which is also corroborated by the NDVI distribution. SSEBop completely missed the peak in 2012 for the shrubland site in Arizona (US-Whs), which may be attributed to having

only a single Landsat 7 satellite in operation. Overall, the results are comparable to earlier reports (e.g., Senay et al., 2013, 2019; Singh et al., 2014, and Velpuri et al., 2013).

Ultimately, the point-based comparison against EC tower data indicates that model accuracy varies from location to location, but on average the model performance is more accurate over croplands compared to forest and grasslands. However, the fact that we observed strong and weak performance within each land cover type indicates the performance of the model may be more tied to the location than cover type. More exploration would be beneficial to understand the spatial variability of model performance by investigating inputs and model
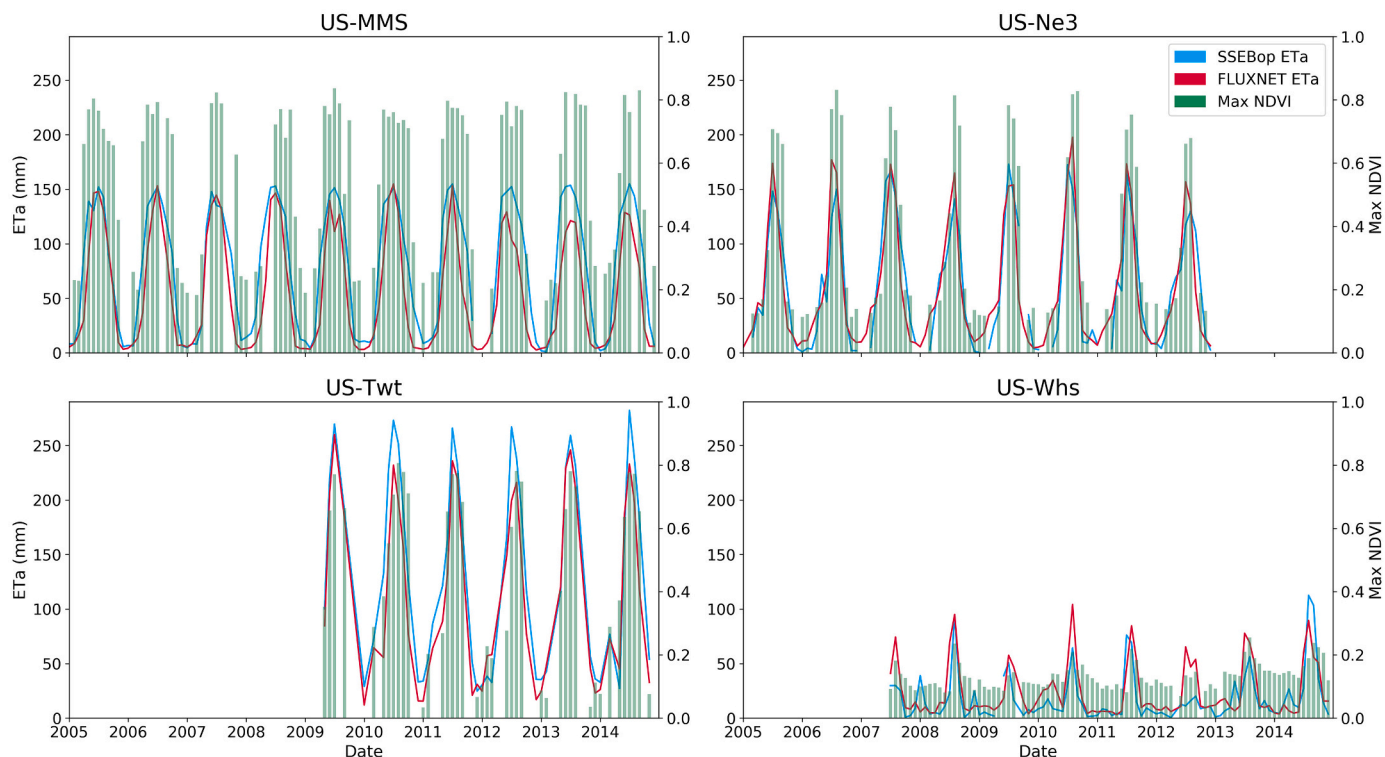
Fig. 7. Temporal comparison of monthly SSEBop ETa, FLUXNET ETa, and NDVI (right axis) for selected FLUXNET sites (US-MMS – deciduous broadleaf forest in Indiana; US-Ne3 – cropland in Nebraska, US-Twt – cropland in California, and US-Whs –shrubland in Arizona).

parameters and conducting sensitivity analysis.

3.3. Performance against water balance ETa

The mean annual HUC8 ETa comparison for the 10-year (2009–2018 water-year) is shown in Fig. 8. The results indicate a good agreement between the SSEBop ET and WBET with an R^2 value of 0.92. The bias on

Fig. 8. Comparison of water-year 2009–2018 mean annual ETa between SSE-Bop and Water Balance (WBET) across HUC8s in the CONUS. The gray line is the 1:1 and the solid dark line is the best fit. The water year for 2009(2018) refers to October 2008(2017) - September 2009(2018) time periods.

annual ETa was 50 mm/yr and RMSE was 123 mm/yr. In comparison to WBET, SSEBop underestimated ETa at the lower ETa rates (regions with <400 mm/yr) and overestimated ETa at higher (>800 mm/yr) ETa rates (Fig. 8). On average, SSEBop overestimated annual ETa by 7% compared to WBET.

The summary of the HUC8 ETa comparison for each water year from 2009 to 2018 is shown in Table 4. The annual mean ETa from SSEBop ranged from 618 mm/yr to 795 mm/yr, and WBET from 625 mm/yr to 764 mm/yr. The R^2 values were above 0.81 for all water years. Bias was within 58 mm/yr and RMSE values were within 161 mm/yr. For most water years (except 2010 and 2011), SSEBop ETa was greater than WBET, and the yearly biases were within 8%. The number of comparable HUC8s (n) varied due to the filtering applied for each water year as presented in Table 4.

HUC8 WBET analysis by hydro-climatic regions indicates varying performances of SSEBop among the six regions. SSEBop overestimated
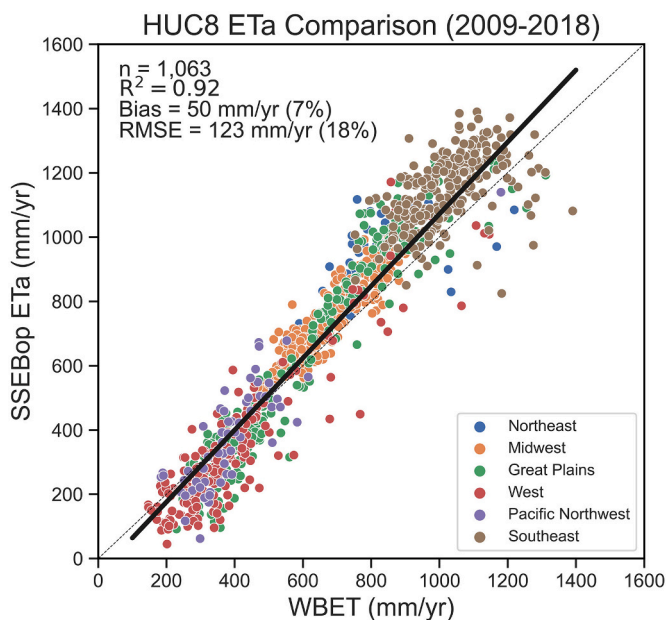
Table 4
Summary of HUC8 ETa comparison between SSEBop and Water Balance (WBET) from the water years 2009 to 2018 using R^2, bias, and RMSE.

Water year	SSEBop ETa mm/yr	WBET mm/yr	n[*]	R^2	Bias mm/yr (%)	RMSE mm/yr (%)
2009	688	676	1104	0.86	12 (2)	125 (19)
2010	671	680	1073	0.83	−10 (−1)	136 (20)
2011	618	625	800	0.81	−7 (−1)	136 (22)
2012	683	666	877	0.89	17 (3)	129 (19)
2013	691	667	1014	0.90	23 (3)	125 (19)
2014	717	689	93	0.89	28 (4)	127 (18)
2015	774	716	896	0.87	58 (8)	149 (21)
2016	795	763	1077	0.86	32 (4)	148 (19)
2017	750	717	918	0.83	33 (5)	161 (22)
2018	787	764	850	0.88	23 (3)	129 (17)

[*] n = number of HUC8s for ETa comparison between SSEBop and WBET. The number varies from year to year due to filtering criteria.

ETa at four regions and underestimated ETa at two regions (Fig. 9). SSEBop tends to overestimate ETa across central and eastern regions of the CONUS and underestimate in the western regions, reinforcing the finding in the EC evaluation that location could be a more important factor to influence the model performance than cover type. On 10-year (2009–2018 water-year) average, the largest overestimation and underestimation bias were at Northeast (16%) and the West (−14%) regions, respectively. The smallest bias was at the Pacific Northwest (−2%) (Fig. 9).

Comparisons of annual ETa for the 10-year average, each water year, and across six different regions show a good agreement between SSEBop ETa and WBET. The performance of SSEBop varied with a distinct regional difference with overestimation in eastern regions with higher ETa values and underestimation in western regions with lower ET rates. Generally, eastern regions of the CONUS receive more precipitation and the ET rates are primarily driven by the available energy to evaporate water from the land surface. In contrast, western regions are drier with less precipitation and thus ET rates are driven by the availability of water at the land surface. As the SSEBop model does not include precipitation or soil moisture information for ETa estimation, the likely reasons for the ETa overestimation in wet regions and underestimation in dry regions are due to the biases in the estimation of model drivers such as land surface temperature (Ts) and ETr and the model parameters such as γ^s and Tc. Particularly, a uniform bias correction for ETr at 0.85 could be responsible for regional variability where a non-uniform bias correction could be more appropriate. Similarly, an under-estimated γ^s parameter could lead to a positive bias while an underestimated Tc could lead to a negative ETa bias.

A few HUC8s in the West region had the largest disagreement up to 400 mm/yr (red points in Fig. 8) between SSEBop ETa and WBET. These HUC8s are clustered in northern California and had a runoff value of zero (0), thus estimating higher WBET. Some of the HUC8s had Q/P values close to the 0.40 threshold, indicating a higher potential for regional groundwater flow, which may have added bias. Limiting the Q/P threshold to 0.30 lowered the mean bias to 3% (17 mm/yr) on 10-year average ETa; however, this substantially reduced the number of comparable HUC8s (630 HUC8s). Thus, due to the lower number of comparable HUC8s, the results were reported for the Q/P ratio greater than 0.40 for covering the majority of HUC8s across different hydro-climatic regions of the CONUS. Both WBET and energy balance (SSEBop) approaches have advantages and limitations for ETa estimation at HUC8 scale. Besides the biases from both approaches, the 10-year average ETa estimations from SSEBop were within 7% for the CONUS, ±8% for each water year, and ± 16% for six regions in comparison to the WBET. These biases are similar to the range of errors reported in the previous studies (Velpuri et al., 2013; Senay et al., 2016) and within the expected bias range of 10–20% from remote sensing-based energy balance algorithms (Allen et al., 2011).

3.4. Anomaly mapping and environmental application

Annual ETa anomalies were calculated as the percent of deviation for each calendar year in relation to the median year (2010–2019) total (Fig. 10). Due to the relatively small number of years (10 years), the median ETa was used from the 2010–2019 annual total ETa (Fig. 4). The calculation of ETa anomalies using relative differences from an average
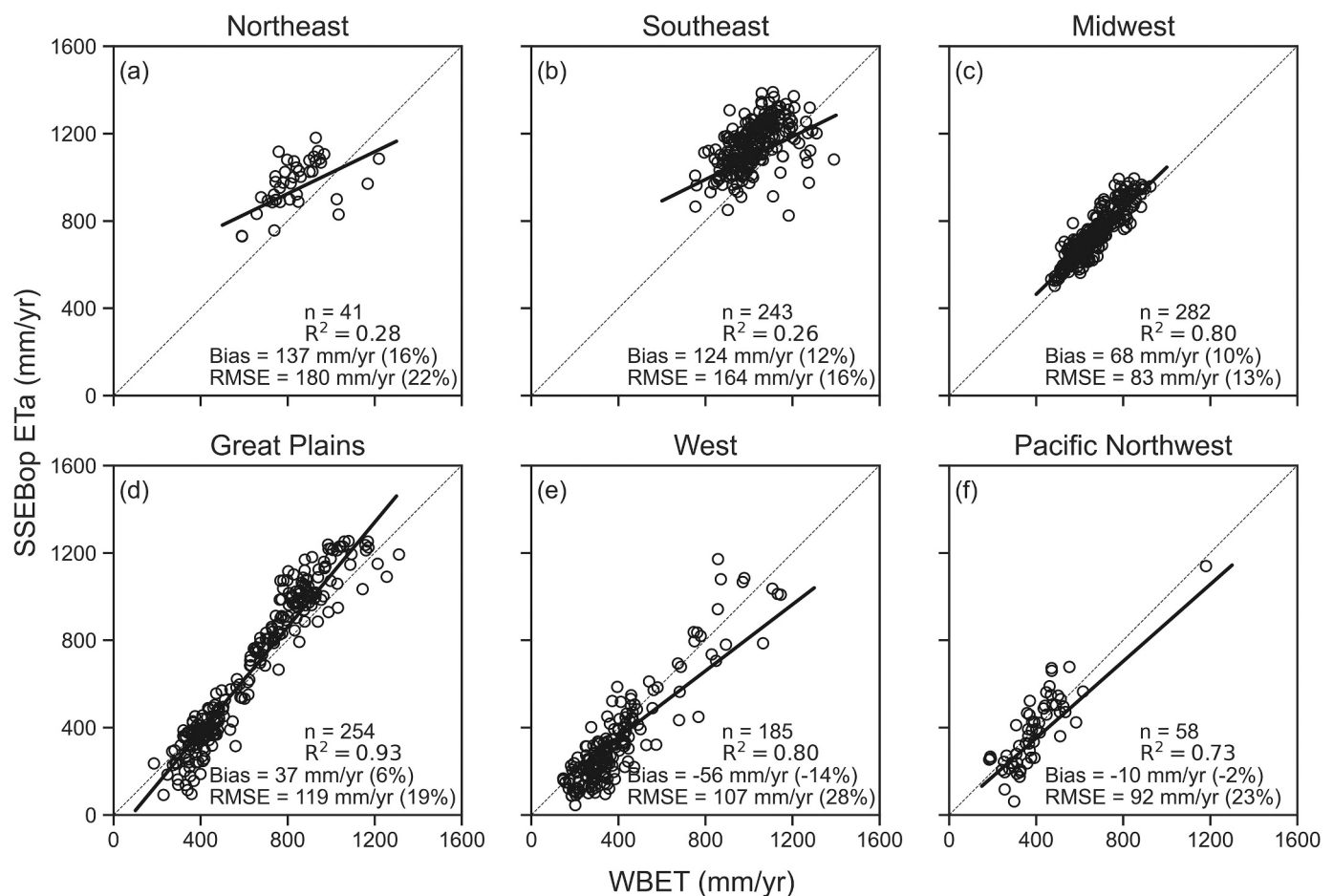

Fig. 9. Comparison of water-year 2009–2018 mean annual ETa between SSEBop and Water Balance (WBET) across HUC8s at six different regions of the conterminous United States.
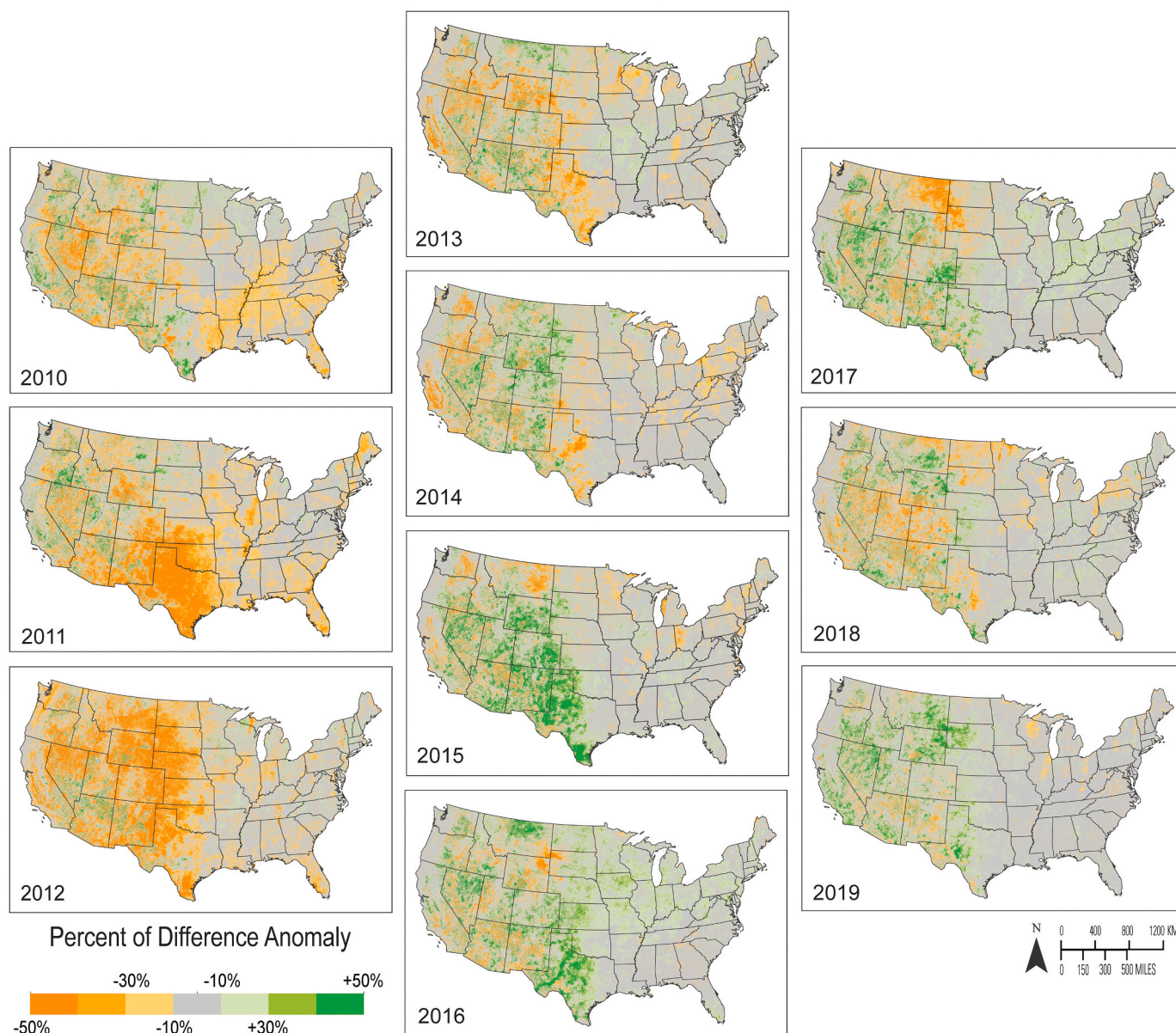
Fig. 10. SSEBop annual (January–December) ETa anomalies from 2010 to 2019 expressed as the percent deviation of each year from the median year. Data were aggregated to 250-m resolution for display.

year is useful for applications in drought monitoring purposes. Anomalies are also useful for field-level land use information, such as cropping practices, and for mapping soil and surface water consumption changes on the landscape, such as from wildfires and other natural disasters.

General spatial patterns of ETa anomalies show relatively drier years from 2010 through 2013 with negative deviation in relation to the median year ETa shown in Fig. 4. Known drought years of 2011 and 2012 are prominently shown in parts of the High Plains in the middle of CONUS (e.g., Texas and Oklahoma). Although such estimates of low ET may signal prolonged water-limited stress conditions on the broader landscape, the degrees of realized effects likely vary with existing drought contingency plans and intervention measures. Reliability of anomalous ET estimates depends on the consistency of clear image data quality and availability from year to year. Due to cloud cover (or snow/ ice) problems, some years may have fewer Landsat images, which required interpolation over longer gaps. This is a potential diagnostic concern for much of the CONUS except in the Southwest and is recognized as an area that would benefit from a separate focus on uncertainty

analysis and detailed gap assessments across large expanses of time and space. Furthermore, with the cloud-based ET production techniques as presented here, opportunities exist for more tailored applications and deeper studies of drought monitoring dynamics using SSEBop from Landsat as a cross-cutting data resource alongside well-known mapping products such as the U.S. Drought Monitor (https://droughtmonitor.unl.edu/Maps/MapArchive.aspx). While illustrations of ET applications are vast, we attempted to center on model product examples with ranges of scope and scale as seen in Figs. 10 and 11. There is tremendous value in national-scale anomaly mapping with Landsat thermal-based ETa information for supporting numerous regional- and field-scale applications that rely on assessment of soil moisture and vegetation conditions from remote observations.

A close-up of ETa and its anomalies around Chico, California, in Fig. 11 shows field-scale details on the effect of alternating irrigation (2018 and 2019) and fire impact in 2019. Fallow fields in 2018 and 2019 (Fig. 11b and c) clearly show negative anomalies capped at −50% deviation, and similarly the effect of the 2018 Camp Fire near Paradise
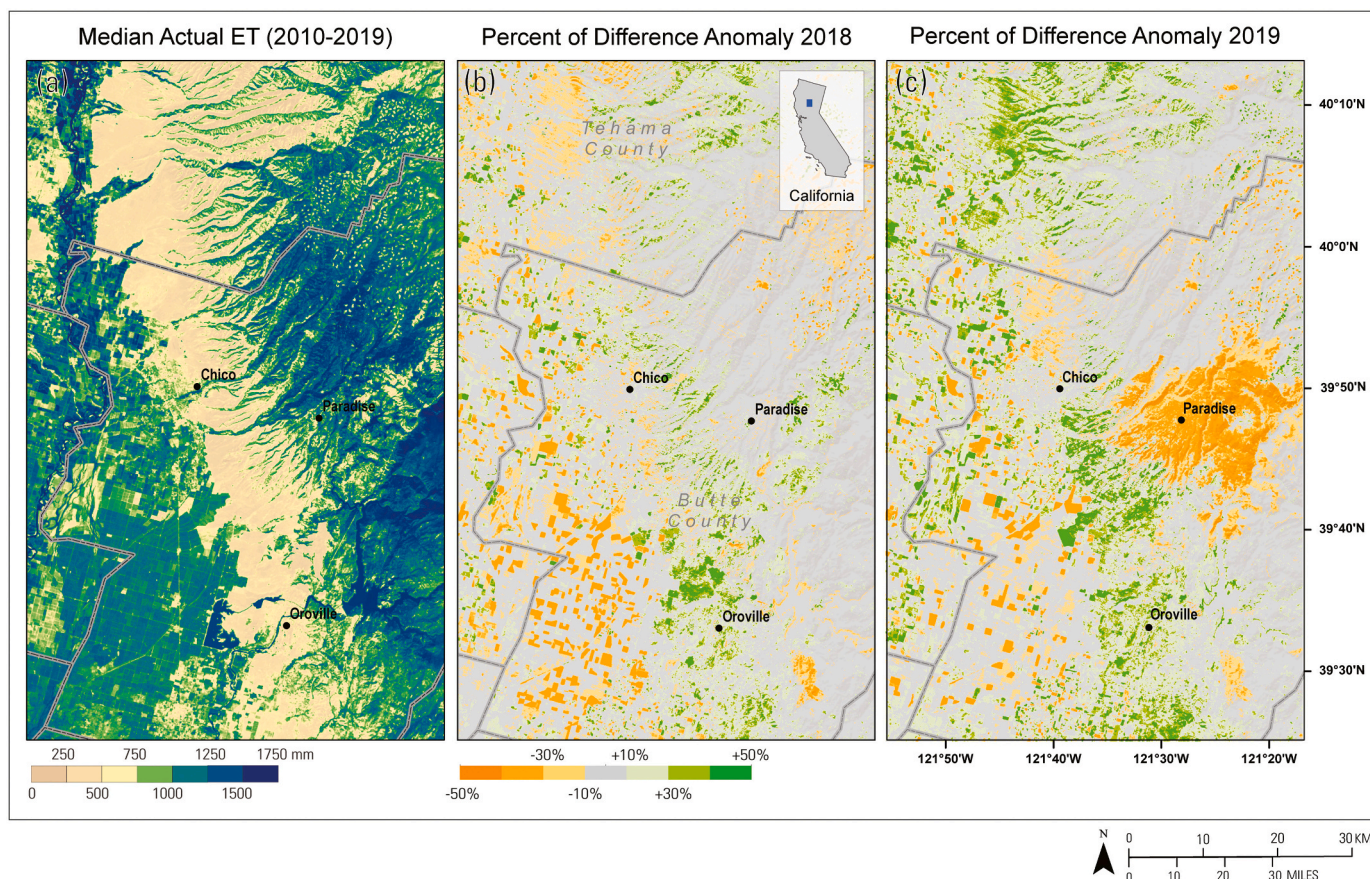
Fig. 11. Illustration of Landsat-resolution median annual ETa (a) and percent of difference ETa anomaly for a location near Chico, California. Negative anomaly ETa results indicate fallow/idle rice fields in the southwest (b, c) and fire burn scar from the historic 2018 Camp Fire near Paradise, California (c).

(Fig. 11c) is shown as negative anomaly in the 2019 annual ETa estimate.

As Fig. 11 shows, Landsat-based ETa is an important dataset for field-scale analysis due to its superior spatial resolution compared to coarser satellites. Particularly, the role of Landsat for field scale water use mapping cannot be matched by existing coarser satellites. But the infrequent observations could create a challenge to develop a drought anomaly product in cloud-prone regions. Despite data frequency concerns, this study demonstrates the capability of Landsat in capturing year to year variability for large area assessment of ETa whether it is for crop water use, drought monitoring, or fire impact mapping. On the other hand, continued research in the integration of Landsat data with MODIS is warranted to improve temporal resolution and with Sentinel-2 to improve both spatial and temporal resolutions as demonstrated by Singh et al. (2020).

3.5. Sources of error

Results presented in this study are subject to uncertainty and bias attributable to multiple factors such as the spatiotemporal variability of Landsat image counts and the distribution of cloud-free images at annual and sub-annual scales, accuracy of the reference ET data, and model parameter accuracies from automated model implementation techniques. These sources are important to recognize when considering applications of ET at any scale. Furthermore, separate studies with due focus and precise analysis of how these errors are affected in different regions would be an important topic for the SSEBop model into the future.

An important and widely recognized challenge with remote sensing data is the varying availability of cloud-free imagery. In this study, we focused on large-scale production and presentation of mapping ETa at the annual time step over CONUS. A summary of annual cloud-free information from Landsat (Fig. 5) shows the number of images ranged from less than 6 in the mountainous, clouded regions to more than 60 images per year in the arid southwest during the 10-year study. Also related, model estimates may at times result in ET artifacts because of errors in the cloud masking algorithm. These are both recognized areas of potential future cloud-impacted evaluation that could contribute to a broader, more detailed uncertainty assessment of seasonal image availability for time integration across large area domains.

The use of a constant 0.85 bias correction factor for the GridMET ETr has a potential to introduce an unknown range of error in different parts of the country as indicated by Blankenau et al. (2020). A spatiotemporally dynamic correction factor would be more appropriate and is expected to improve the results. Furthermore, the study used a climatology ETr that could introduce random errors on a given day, but its effect is minimized at monthly and annual time scales. However, bias errors will persist at longer time scales, with a larger effect during extreme dry/clear-sky or wet/cloudy years that are different from the climatology.

The Ts is generated by using NDVI thresholds for emissivity components as implemented by Singh et al. (2014) and Senay et al. (2016). Exploratory comparison (data not presented) of our Ts against the Landsat Collection 2 (C2) Ts from USGS Earth Resources Observation and Science (https://www.usgs.gov/core-science-systems/nli/landsat/landsat-collection-2-level-2-science-products) has shown that the C2 Ts seems to show wider dynamic range than the C1-based Ts used in this study in parts of central and eastern CONUS and more comparable in the western CONUS. Future application of the SSEBop method will use the C2 Ts which is expected to improve its performance. The Landsat C2 was not available on GEE for timely use of the dataset in this study.

In addition to model inputs, the two model parameters γ^s and Tc tend to create directional biases, but not random error for a given location. The optimization algorithm for these model parameters is sensitive to their respective calibration procedures and underlying assumptions. For example, the Tc depends on the establishment of the cold/wet pixel based on using a high NDVI (≥ 0.7) threshold for every 5-km grid cell. This could introduce an overestimation bias if most of the calibration pixels are barely meeting the minimum threshold, because slightly stressed vegetation pixels could be assumed to experience a maximum ET. Image inspections have shown up to 4 degrees (K) difference in Ts values between NDVI = 0.7 and NDVI = 0.9, which could introduce a large bias, up to 20% of maximum ET on a summer condition. The absence of such high NDVI pixels in the cluster of calibration points is usually an issue in less vegetated arid and semi-arid regions and outside of typical growing seasons. Similarly, the accuracy of the γ^s ($1/dT$) parameter depends on the correctness of the gray-sky radiation and the calibration process in determining the r_{ah} parameter. A higher (over-estimated) dT will lead to an ETa overestimation and vice versa, but its effect is more pronounced in low ET pixels, assuming the Tc is correctly set. Senay et al. (2011) reported that a 10% error in dT will result in a 30% relative error for pixels with ETf = 0.25, but only introduce a 3% relative error for pixels with ETf = 0.75. From the HUC-based water balance study, we have noticed a general underestimation in the arid West/Pacific Northwest and overestimation in the Southeast, which could be related to a lower dT that may underestimate and disproportionally affect the low ET areas in the arid regions and using a 0.7 NDVI c factor threshold that could lead to overestimation in the vegetated Southeast. Future work could include a sensitivity analysis to improve the optimization of these two parameters in diverse agro-climatic regions.

4. Conclusions

The main objectives of this study were to implement the SSEBop model in the GEE cloud computing environment to model wall-to-wall ETa for the CONUS, describe model parameter improvements, and evaluate the results using independent data sources along with presenting an application use case with ETa anomalies.

The study has demonstrated the capability and strength of the GEE platform to process and model CONUS-wide SSEBop ETa at the Landsat scale, overcoming earlier challenges and limitations on large data storage and extended computational time, processing ~15,000 images for CONUS within one week. The increased computational efficiency allowed for iterative model refinement and reparameterization and better time-integrated per-pixel interpolation methods across complete Landsat collections, improving the overall model performance. Furthermore, use of GEE has led to greater data inquiry with faster insights and generated responsive solutions with dedicated APIs leading to ongoing external collaboration frameworks essential to the future of science applications at increasing scales.

Evaluation of ETa estimates against EC tower and Water Balance ETa techniques demonstrated that model accuracy appears dependent on specific locations and regions rather than cover type with a general underestimation in low ETa regions ($<~400$ mm/yr) and overestimation in high ETa regions ($> ~ 800$ mm/yr) but with an average annual bias of 7% compared with WBET. However, EC tower evaluation showed that SSEBop, on average, performed better over croplands than over forest and grasslands areas. There was large variability in performance within each cover type indicating the importance of improving data inputs and parameters over local conditions. Future modeling efforts could address these challenges for more consistent and accurate ETa spatial representation.

Landsat-based ETa results from this study were comparable to MODIS-based results in terms of accuracy metrics such as R^2 and RMSE, but Landsat provides a superior fine detailed information at the field scale that was not possible to achieve at the MODIS scale. It would not be

surprising to obtain a weaker performance with Landsat when using seasonal and yearly totals due to uncertainty in interpolation to fill missing Landsat pixels due to cloud cover. The encouraging performance of temporally aggregated ETa from Landsat for drought and fire impacts is indicative of the possibility to produce fine resolution time series mapping, monitoring, and assessment products for land and water resources managers.

Cloud computing of the Landsat image archive combined with other satellite, climate, and weather data, creates new opportunities for assessing ET model behavior and uncertainty, and ultimately providing the ability for more robust operational monitoring and understanding of water use at the field level. These capabilities to rapidly process large volumes of remote sensing datasets can provide answers to more challenging hydrologic modeling questions than ever before.

The power of cloud computing could be extended to merge Landsat data with multiple satellite sources that can improve the temporal frequency with comparable number of quality images over multiple years to create consistent and reliable seasonal ETa for field-scale assessment and trend analysis over large areas such as CONUS and beyond.

Credit author statement

Gabriel Senay is responsible for conceptualization, writing, supervision, and fund acquisition; MacKenzie Friedrichs is responsible for GEE software implementation of the SSEBop code, writing, and editing; Charles Morton is responsible for GEE SSEBop code development and review; Gabriel Parrish is responsible for SSEBop methodology development on the gridded c implementation and review; Matthew Schauer is responsible for the EC tower-based validation and writing; Kul Khand is responsible for validation using water balance techniques and writing; Stefanie Kagone is responsible on methods development on the dT parameter, data curation, and visualization; Olena Boiko is responsible for NDVI analysis, supporting the validation using EC tower data, and dT parameter development; Justin Huntington is responsible for supervision of GEE SSEBop development and review of manuscript.

Declaration of Competing Interest

The authors declare that they have no known competing financial interests or personal relationships that could have appeared to influence the work reported in this paper.

References

Abatzoglou, J.T., 2013. Development of gridded surface meteorological data for ecological applications and modelling. Int. J. Climatol. 33, 121–131.

Alemohammad, S.H., Fang, B., Konings, A.G., Aires, F., Green, J.K., Kolassa, J., Miralles, D., Prigent, C., Gentine, P., 2017. Water, energy, and carbon with artificial neural networks (WECANN): a statistically based estimate of global surface turbulent fluxes and gross primary productivity using solar-induced fluorescence. Biogeosciences 14, 4101–4124.

Allen, R.G., Howell, T.A., Pruitt, W.O., Walter, I.A., Jensen, M.E., 1991. Lysimeters for Evapotranspiration and Environmental Measurements. American Society of Civil Engineers (ASCE), New York.

Allen, R.G., Pereira, L.S., Raes, D., Smith, M., 1998. Crop Evapotranspiration-Guidelines for Computing Crop Water Requirements-FAO Irrigation and Drainage Paper 56, 300. FAO, Rome, p. D05109.

Allen, R.G., Tasumi, M., Morse, A., Trezza, R., Wright, J.L., Bastiaanssen, W., Kramber, W., Lorite, I., Robison, C.W., 2007. Satellite-based energy balance for mapping evapotranspiration with internalized calibration (METRIC)—applications. J. Irrig. Drain. Eng. 133, 395–406.

Allen, R.G., Pereira, L.S., Howell, T.A., Jensen, M.E., 2011. Evapotranspiration information reporting: I. Factors governing measurement accuracy. Agric. Water Manag. 98, 899–920.

Anderson, M.C., Norman, J.M., Mecikalski, J.R., Otkin, J.A., Kustas, W.P., 2007. A climatological study of evapotranspiration and moisture stress across the continental United States based on thermal remote sensing: 1. Model formulation. J. Geophys. Res. 112, D10117.

Baldocchi, D., Falge, E., Gu, L., Olson, R., Hollinger, D., Running, S., Anthoni, P., Bernhofer, C., Davis, K., Evans, R., 2001. FLUXNET: a new tool to study the temporal and spatial variability of ecosystem-scale carbon dioxide, water vapor, and energy flux densities. Bull. Am. Meteorol. Soc. 82, 2415–2434.

Bawa, A., Senay, G.B., Kumar, S., 2020. Regional crop water use assessment using Landsat-derived evapotranspiration. Hydrol. Process. 35, e14015.

Blankenau, P.A., Kilic, A., Allen, R., 2020. An evaluation of gridded weather data sets for the purpose of estimating reference evapotranspiration in the United States. Agric. Water Manag. 242, 106376.

Bowen, I.S., 1926. The ratio of heat losses by conduction and by evaporation from any water surface. Phys. Rev. 27, 779.

Brakebill, J.W., Wolock, D.M., Terziotti, S., 2011. Digital hydrologic networks supporting applications related to spatially referenced regression modeling 1. JAWRA J. Am. Water Resour. Assoc. 47, 916–932.

Choi, M., Kustas, W.P., Anderson, M.C., Allen, R.G., Li, F., Kjaersgaard, J.H., 2009. An intercomparison of three remote sensing-based surface energy balance algorithms over a corn and soybean production region (Iowa, US) during SMACEX. Agric. For. Meteorol. 149, 2082–2097.

Daly, C., Neilson, R.P., Phillips, D.L., 1994. A statistical-topographic model for mapping climatological precipitation over mountainous terrain. J. Appl. Meteorol. Climatol. 33, 140–158.

FAO, 2018. WaPOR Database Methodology: Level 1. Remote Sensing for Water Productivity Technical Report: Methodology Series Rome, FAO, Licence: CC BY-NC-SA 3.0 IGO.

Farr, T.G., Rosen, P.A., Caro, E., Crippen, R., Duren, R., Hensley, S., Kobrick, M., Paller, M., Rodriguez, E., Roth, L., 2007. The shuttle radar topography mission. Rev. Geophys. 45.

Fisher, J.B., Tu, K.P., Baldocchi, D.D., 2008. Global estimates of the land–atmosphere water flux based on monthly AVHRR and ISLSCP-II data, validated at 16 FLUXNET sites. Remote Sens. Environ. 112, 901–919.

Gorelick, N., Hancher, M., Dixon, M., Ilyushchenko, S., Thau, D., Moore, R., 2017. Google earth engine: planetary-scale geospatial analysis for everyone. Remote Sens. Environ. 202, 18–27.

Guerschman, J.P., Van Dijk, A.I., Mattersdorf, G., Beringer, J., Hutley, L.B., Leuning, R., Pipunic, R.C., Sherman, B.S., 2009. Scaling of potential evapotranspiration with MODIS data reproduces flux observations and catchment water balance observations across Australia. J. Hydrol. 369, 107–119.

Homer, C., Dewitz, J., Yang, L., Jin, S., Danielson, P., Xian, G., Coulston, J., Herold, N., Wickham, J., Megown, K.J.P.E., et al., 2015. Completion of the 2011 National Land Cover Database for the conterminous United States–representing a decade of land cover change information. Photogramm. Eng. Remote Sens. 81, 345–354.

Huntington, Justin, Hegewisch, Katherine, Daudert, Britta, Morton, Charles, Abatzoglou, John, McEvoy, Daniel, Erickson, Tyler, 2017. Climate Engine: Cloud computing and visualization of climate and remote sensing data for advanced natural resource monitoring and process understanding. Bulletin of the American Meteorological Society 98 (11), 2397–2410. https://doi.org/10.1175/BAMS-D-15-00324.1.

Irmak, A., Ratcliffe, I., Ranade, P., Hubbard, K.G., Singh, R.K., Kamble, B., Kjaersgaard, J., 2011. Estimation of land surface evapotranspiration with a satellite remote sensing procedure. Great Plains Res. 73–88.

Jiang, L., Islam, S., 2001. Estimation of surface evaporation map over southern Great Plains using remote sensing data. Water Resour. Res. 37, 329–340.

Jiang, C., Guan, K., Pan, M., Ryu, Y., Peng, B., Wang, S., 2020. BESS-STAIR: a framework to estimate daily, 30 m, and all-weather crop evapotranspiration using multi-source satellite data for the U.S. Corn Belt. Hydrol. Earth Syst. Sci. 24, 1251–1273.

Ke, Y., Im, J., Park, S., Gong, H., 2017. Spatiotemporal downscaling approaches for monitoring 8-day 30 m actual evapotranspiration. ISPRS J. Photogramm. Remote Sens. 126, 79–93.

Khand, K., Numata, I., Kjaersgaard, J., Vourlitis, G.L., 2017. Dry season evapotranspiration dynamics over human-impacted landscapes in the southern Amazon using the Landsat-based METRIC model. Remote Sens. 9 (7), 706.

Kustas, W.P., Norman, J.M., 2000. A two-source energy balance approach using directional radiometric temperature observations for sparse canopy covered surfaces. Agron. J. 92, 847–854.

Li, Z., Liu, X., Ma, T., Kejia, D., Zhou, Q., Yao, B., Niu, T., 2013. Retrieval of the surface evapotranspiration patterns in the alpine grassland-wetland ecosystem applying SEBAL model in the source region of the yellow river, China. Ecol. Model. 270, 64–75.

Melton, F.S., Huntington, H., Grimm, R., Herring, J., Hall, M., Rollison, D., Erickson, T., et al., 2021. OpenET: filling a critical data gap in water management for the Western United States. J. Am. Water Resour. Assoc. 1–24. https://doi.org/10.1111/1752-1688.12956.

Mu, Q., Zhao, M., Running, S.W., 2011. Improvements to a MODIS global terrestrial evapotranspiration algorithm. Remote Sens. Environ. 115, 1781–1800.

Nagler, P.L., Brown, T., Hultine, K.R., Bean, D.W., Dennison, P.E., Murray, R.S., Glenn, E. P., 2012. Regional scale impacts of Tamarix leaf beetles (Diorhabda carinulata) on the water availability of western US rivers as determined by multi-scale remote sensing methods. Remote Sens. Environ. 118, 227–240.

Numata, I., Khand, K., Kjaersgaard, J., Cochrane, M.A., Silva, S.S., 2017. Evaluation of Landsat-based METRIC modeling to provide high-spatial resolution evapotranspiration estimates for Amazonian forests. Remote Sens. 9 (1), 46.

Pastorello, G., Trotta, C., Canfora, E., Chu, H., Christianson, D., Cheah, Y.-W., Poindexter, C., Chen, J., Elbashandy, A., Humphrey, M., 2020. The FLUXNET2015 dataset and the ONEFlux processing pipeline for eddy covariance data. Sci. Data 7, 1–27.

Schauer, M., Senay, G.B., 2019. Characterizing crop water use dynamics in the Central Valley of California using Landsat-derived evapotranspiration. Remote Sens. 11, 1782.

Seaber, P.R., Kapinos, F.P., Knapp, G.L., 1987. Hydrologic Unit Maps.

Senay, G.B., 2008. Modeling landscape evapotranspiration by integrating land surface phenology and a water balance algorithm. Algorithms 1 (2), 52–68.

Senay, G.B., 2018. Satellite psychrometric formulation of the operational simplified surface energy balance (SSEBop) model for quantifying and mapping evapotranspiration. Appl. Eng. Agric. 34, 555–566.

Senay, G.B., Budde, M.E., Verdin, J.P., 2011. Enhancing the simplified surface energy balance (SSEB) approach for estimating landscape ET: validation with the METRIC model. Agric. Water Manag. 98, 606–618.

Senay, G.B., Bohms, S., Singh, R.K., Gowda, P.H., Velpuri, N.M., Alemu, H., Verdin, J.P., 2013. Operational evapotranspiration mapping using remote sensing and weather datasets: a new parameterization for the SSEB approach. J. Am. Water Resour. Assoc. 49, 577–591.

Senay, G.B., Friedrichs, M., Singh, R.K., Velpuri, N.M., 2016. Evaluating Landsat 8 evapotranspiration for water use mapping in the Colorado River basin. Remote Sens. Environ. 185, 171–185.

Senay, G.B., Schauer, M., Friedrichs, M., Velpuri, N.M., Singh, R.K., 2017. Satellite-based water use dynamics using historical Landsat data (1984–2014) in the southwestern United States. Remote Sens. Environ. 202, 98–112.

Senay, G.B., Schauer, M., Velpuri, N.M., Singh, R.K., Kagone, S., Friedrichs, M., Litvak, M.E., Douglas-Mankin, K.R., 2019. Long-term (1986–2015) crop water use characterization over the upper Rio Grande Basin of United States and Mexico using landsat-based evapotranspiration. Remote Sens. 11, 1587.

Senay, G.B., Kagone, S., Velpuri, N.M., 2020. Operational global actual evapotranspiration: development, evaluation and dissemination. Sensors 20, 1915.

Senay, G.B., Friedrichs, M., Parrish, G.E., Schauer, M., Khand, K., Kagone, S., 2021a. Annual SSEBop ET Rasters at Landsat Scale from 2010-2019 for the CONUS: U.S. Geological Survey Data Release. https://doi.org/10.5066/P9SJLMAQ.

Senay, G.B., Friedrichs, C., Parrish, G.E., Schauer, M., Khand, K., Kagone, S., Boiko, O., 2021b. Actual Evapotranspiration at Landsat Scale for CONUS from 2010-2019: U.S. Geological Survey Data Release. https://doi.org/10.5066/P9FZCZ78.

Singh, R.K., Senay, G.B., Velpuri, N.M., Bohms, S., Verdin, J.P., 2014. On the downscaling of actual evapotranspiration maps based on combination of MODIS and Landsat-based actual evapotranspiration estimates. Remote Sens. 6, 10483–10509.

Singh, R.K., Khand, K., Kagone, S., Schauer, M., Senay, G.B., Wu, Z., 2020. A novel approach for next generation water-use mapping using Landsat and Sentinel-2 satellite data. Hydrol. Sci. J. 65, 2508–2519.

Sun, Z., Wei, B., Su, W., Shen, W., Wang, C., You, D., Liu, Z., 2011. Evapotranspiration estimation based on the SEBAL model in the nansi lake wetland of China. Math. Comput. Model. 54 (3–4), 1086–1092.

Sun, L., Anderson, M.C., Gao, F., Hain, C., Alfieri, J.G., Sharifi, A., McCarty, G.W., Yang, Y., Yang, Y., Kustas, W.P., 2017. Investigating water use over the Choptank River Watershed using a multisatellite data fusion approach. Water Resour. Res. 53, 5298–5319.

Thornton, P., Thornton, M., Mayer, B., Wei, Y., Devarakonda, R., Vose, R., Cook, R., 2016. Daymet: Daily Surface Weather Data on a 1-Km Grid for North America, Version 3. ORNL DAAC, Oak Ridge, Tennessee, USA.

Velpuri, N.M., Senay, G.B., Singh, R.K., Bohms, S., Verdin, J.P., 2013. A comprehensive evaluation of two MODIS evapotranspiration products over the conterminous United States: using point and gridded FLUXNET and water balance ET. Remote Sens. Environ. 139, 35–49.

Vertessy, R., Hatton, T., Reece, P., O'sullivan, S., Benyon, R., 1997. Estimating stand water use of large mountain ash trees and validation of the sap flow measurement technique. Tree Physiol. 17, 747–756.

Yang, Y., Anderson, M.C., Gao, F., Wardlow, B., Hain, C.R., Otkin, J.A., Alfieri, J., Yang, Y., Sun, L., Dulaney, W., 2018. Field-scale mapping of evaporative stress indicators of crop yield: an application over Mead, Nebraska, USA. Remote Sens. Environ. 210, 387–402.

Yang, Y., Anderson, M., Gao, F., Hain, C., Noormets, A., Sun, G., Sun, L., 2020. Investigating impacts of drought and disturbance on evapotranspiration over a forested landscape in North Carolina, USA using high spatiotemporal resolution remotely sensed data. Remote Sens. Environ. 238, 111018.

Zheng, C., Jia, L., Hu, G., Lu, J., Wang, K., Li, Z., 2016. Global evapotranspiration derived by ETMonitor model based on earth observations. In: 2016 IEEE International Geoscience and Remote Sensing Symposium (IGARSS), pp. 222–225.